*J. Fluid Mech.* (2006), *vol.* 552, *pp.* 189–227.  
doi:10.1017/S0022112005008608 Printed in the United Kingdom

# Spatial versus temporal instabilities in a parametrically forced stratified mixing layer

By A. YU. GELFGAT† AND E. KIT

School of Mechanical Engineering, Faculty of Engineering, Tel-Aviv University, Ramat Aviv, 69978, Israel

(Received 6 December 2004 and in revised form 9 June 2005)

A spatial instability of parametrically excited stratified mixing layer flows is considered together with the related temporal instability problem. A relatively simple iteration procedure yielding solutions of both temporal and spatial problems is proposed. Using this procedure a parametric analysis of the temporal and spatial Kelvin–Helmholtz and Holmboe instabilities is performed and characteristic features of the instabilities are compared. Both inviscid and viscous models are considered. The parametric dependence on the mixing layer thickness and on the Richardson and Reynolds numbers is studied. It is shown that in the framework of this study the Gaster transformation is valid for the Kelvin–Helmholtz instability, but cannot be applied to the Holmboe one. The neutral stability curves are calculated for the viscous flow case. It is found that the transition between Kelvin–Helmholtz and Holmboe instabilities is continuous in the spatial case and in the temporal case occurs via the codimension-two bifurcation at which a complex pair of the leading eigenvalues merges into a multiple real eigenvalue. It is also found that for the same governing parameters the spatial upstream and downstream Holmboe waves have different amplification rates and different absolute phase velocities, with larger difference observed at larger Richardson numbers. It is shown that at large Richardson and small Reynolds numbers the primary temporal and spatial instabilities set in as a three-dimensional oblique Holmboe wave.

## 1. Introduction

Most computational modelling of instabilities and nonlinear supercritical regimes developing in initially parallel shear flows is performed using the so-called temporal formulation, in which the spatial flow periodicity is fixed and temporal evolution of the perturbations is studied. On the other hand, most experiments, as well as similar flows appearing in nature and technical applications, relate to so-called spatial instability. Here flow originates at a certain point and the instability develops in space, in the direction of mean velocity. In the present paper we consider a case in which the spatial instability of a plane parallel shear flow is excited parametrically by a time-oscillating perturbation having a certain frequency. Considering this particular case of instability excitation, we describe a novel procedure that allows computation of both temporal and spatial instabilities, and, consequently, for the comparison between them.

To distinguish between the spatial and temporal instabilities or, to be more precise, between spatially and temporally growing disturbances, we consider the basic

† Author to whom correspondence should be addressed: gelfgat@eng.tau.ac.il

plane-parallel flow $U(y)$ and the general form of its perturbation $A(y)\exp[\mathrm{i}(\alpha x + \alpha_z z - \omega t)]$. Assuming that Squire's theorem applies (Yih 1955; Koppel 1964), it is sufficient to consider only two-dimensional perturbations, i.e. the perturbations with $\alpha_z = 0$. The parameters $\alpha = \alpha_r + \mathrm{i}\alpha_i$ and $\omega = \omega_r + \mathrm{i}\omega_i$ are generally complex. The temporal instability corresponds to fixed real $\alpha = \alpha_r$, which then plays the role of the spatial wavenumber of the perturbation, and complex $\omega$ such that $\omega_i > 0$. Here $\omega_i$ is the amplification rate of a temporally growing disturbance and $\omega_r$ is the circular frequency of the disturbance. The spatial instability corresponds to fixed real $\omega = \omega_r$ and complex $\alpha$ such that $\alpha_i < 0$. Here, $-\alpha_i$ is the amplification rate of a perturbation growing in the positive direction of the axis $x$.

The first attempt to study the relation between spatial and temporal instabilities was made by Gaster (1962). Considering a general form of the relations $\alpha = \alpha(\omega)$ and $\omega = \omega(\alpha)$ in the complex plane, assuming them to be analytical functions and their derivatives $\partial\omega_i/\partial\alpha_r$ and $\partial\alpha_i/\partial\omega_r$ to be small, he showed that that if $\omega_{r,spatial} = \omega_{r,temporal}$ (or $\alpha_{r,spatial} = \alpha_{r,temporal}$) is explicitly chosen then $\alpha_{r,spatial} \approx \alpha_{r,temporal}$ (or $\omega_{r,spatial} \approx \omega_{r,temporal}$), and then the temporal and spatial amplification rates are connected by the group velocity $c_g$

$$\frac{\omega_{i,temporal}}{\alpha_{i,spatial}} = -c_g, \quad c_g = \frac{\partial\omega_r}{\partial\alpha_r}. \tag{1}$$

Nayfeh & Padhye (1979) derived a similar transformation using the method of multiple scales and illustrated its applicability to the Blasius velocity profile. However, it was shown that relation (1) is not applicable in many other cases. Thus, Betchov & Criminale (1966) considered a jet profile and showed that the dispersion relation can become singular when the wave speed is equal to the group velocity. These singularities were discussed in Gaster (1968). Peng & Williams (1987) argued that the error of both transformations grows with the increase of the ratio $\alpha_i/\alpha_r$. Roychowdhury & Sreedhar (1992) showed that the Gaster transformation (1) remains valid only in the vicinity of the point $\alpha_r = \alpha_i = 0$.

The restrictions on the Gaster transformation were partially removed by Monkewitz & Huerre (1982). They considered expansions of the dispersion relation in a power series of the velocity ratio parameter $\lambda = (U_{max} - U_{min})/(U_{max} + U_{min})$, which was assumed to be small. Here $U_{min}$ and $U_{max}$ are the minimal and the maximal values of the basic velocity profile $U(y)$. In the power series derived by Monkewitz & Huerre (1982) the Gaster transformation (1) appears as a zero-order term and therefore is applied only to small $\lambda$. Peltier & Scinocca (1990) found a significant difference between the temporal and spatial instabilities, which they attributed to the breakdown of the Gaster transformation (1). Ortiz, Chomaz & Loiseleux (2002) studied the validity of Gaster's transformation for inviscid stratified mixing layer flow with piecewise velocity and stepwise density profiles and showed that it "predicts remarkably well the spatial instability except close to the absolute-convective thresholds". In this study we propose a way to compare quantitatively the temporal and spatial instabilities, which also allows us to check the applicability of the Gaster transformation.

The linear stability characteristics of the spatial modes appear to be important far beyond the small disturbance limit. Freymuth (1966) for boundary layer flow and Gaster, Kit & Wygnanski (1985) for the mixing layer showed that the experimentally measured amplitude and phase of the first Fourier harmonic of developed parametrically excited turbulent flow coincides with the amplitude and phase of the leading spatially growing eigenfunction. These results were confirmed in experimental

studies of Wygnanski, Champagne & Marasli (1986), Cohen & Wygnanski (1987) and Weisbrot & Wygnanski (1988) for wakes, axisymmetric jets, and mixing layers, respectively. The numerical results of Ghoniem & Ng (1987) and Soh (1994) support this for the spatial formulation, and the results of Smyth, Klaasen & Peltier (1988) and Scinocca (1995) for the temporal one. Smyth, Moum & Caldwell (2001) provided additional arguments showing that turbulent flows in the ocean can be caused by shear instability similar to one observed in mixing layers.

The stability analysis for the spatially growing perturbations results in a nonlinear eigenvalue problem for the complex spatial wavenumber (spatial amplification rate). The temporal problem, however, can be reduced to a linear eigenproblem, which can be treated by standard means of linear algebra. The amplification rates and patterns of spatially developing perturbations were calculated by Michalke (1965), Monkewitz & Huerre (1982), Gaster *et al.* (1985), Lie & Riahi (1988), Sutherland & Peltier (1992), Wilson & Demuren (1996), and Ortiz *et al.* (2002). It is not quite clear how the parameters should be chosen to compare quantitatively between the two types of the instability. Therefore, most comparisons reported (e.g. Michalke 1965; Miksad 1972) were mainly qualitative. Ortiz *et al.* (2002) made a quantitative comparison using the analytical dispersion relation known for ideal fluid flow with a piecewise velocity profile; however a certain lack of clarity still remains if more general models (e.g. continuous profiles of density and velocity, viscous flow) are considered. This lack of clarity can be resolved if one considers a parametric excitation of an instability, in which the spatial instability is excited by a single-frequency perturbation. Then, the perturbation frequency for the spatial formulation is fixed. The mean velocity of the mixing layer multiplied by the temporal period of the excitation yields the initial spatial period of the iteration procedure. The temporal problem formulated for this spatial period can be directly and quantitatively compared with the spatial one. Such a comparison is one of the goals of the present study.

Our motivation to compare the temporal and spatial instabilities quantitatively follows, in particular, from a necessity to compare experimental and numerical results. The temporal problem can be studied in two-dimensional (e.g. Patnaik, Sherman Corcos 1976; Smyth *et al.* 1988; Mallier 1995; Staquet 1995; Reinaud, Joly & Chassaing 2000; Miller, Harstad & Bellan 2001; Smyth 2003, 2004), as well as in three-dimensional formulations (e.g. Smyth & Peltier 1990, 1991, 1994; Knio & Ghoniem 1991; Comte *et al.* (1989); Scinocca 1995; Cortesi, Yadigaroglu & Banerjee 1998; Cortesi *et al.* 1999; Caulfield & Peltier 2000; Staquet 2000; Smyth & Moum 2000*a*, *b*; Balaras, Piomelli & Wallace 2001; Peltier & Caulfield 2003; Smyth & Winters 2003; Smyth 2004). Stability of finite-amplitude two-dimensional Kelvin-Helmholz billows and their transition to a three-dimensional state was studied by Klaassen & Peltier (1995). Numerical modelling of the spatial problem requires much longer computational domains to allow the spatial development of the flow. Such studies, e.g. Ghoniem & Ng (1987), Korczak & Wessel (1989), Pruett (1989), Comte *et al.* (1989), Peltier & Scinocca (1990), Soh (1994), Wilson & Demuren (1996), Reinaud *et al.* (2000), have been carried out only in the two-dimensional formulation. Three-dimensional numerical studies of spatially developing instabilities are extremely difficult because a combination of long computational domains with high numerical accuracy leads to enormously large computations. An attempt to approach this problem using the technique of large-eddy simulation (LES) was made by Vreman, Guerts & Kuerten (1997).

One of the goals of this paper is a parametric study of the dependence of the spatial and temporal instabilities on the governing parameters of the problem. Such studies

have been conducted earlier (e.g. Davis & Peltier 1977; Balsa 1987; Nishida & Yoshida 1987, 1990; Smyth & Peltier 1989; Peltier & Scinocca 1990; Chen & Jirka 1998; Ortiz *et al.* 2002; Hogg & Ivey 2003 and references therein); however not all possible questions were answered, especially regarding the spatial instability. Here we study, in particular, how transitions between the Kelvin-Helmholtz (K-H) and Holmboe instabilities take place in the temporal and spatial problems and how the features of the instabilities depend on the Reynolds and Richardson numbers. According to our findings the transition from *temporal* K-H to temporal Holmboe instability takes place via the codimension- two Takens–Bogdanov bifurcation (Kuznetsov 2004), which is in agreement with the earlier analytical (e.g. Holmboe 1962; Ortiz *et al.* 2002) and numerical (e.g. Smyth & Peltier 1989) results. This bifurcation is characterized by a merging of two monotonic K-H modes with the simultaneous appearance of a conjugated pair of Holmboe modes. We show additionally that in the space of Richardson number, Reynolds number and layer thickness, there exists a parametric surface across which this Takens–Bogdanov bifurcation takes place.

Our results related to the *spatial* instability show that conversely to the temporal case, the transition between spatial K-H and spatial Holmboe instabilities is continuous. This is consistent with the observation of Pawlak & Armi (1998) who noticed that there is no clearly defined criterion that allows one to distinguish between the spatial K-H and Holmboe modes. Our results show that both instabilities are excited by the same perturbation mode, which changes parametrically with a certain governing parameter, e.g. Richardson number or layer thickness. Defining the absolute phase velocity as the difference between the actual phase velocity and the average velocity of basic flow we observe a steep increase of the absolute phase velocity from very small, characteristic of the K-H modes, to the significantly larger absolute phase velocity of the Holmboe modes. Such continuous transitions of the spatial instabilities were observed before for inviscid flow with the neglected density diffusion by Pawlak & Armi (1998) and by Ortiz *et al.* (2002) and the transition region was attributed to so-called 'hybrid modes'. Here we show that the transition remains continuous also for viscous flows with accounting for the density diffusion.

Another interesting observation relates to the amplification rates and absolute phase velocities of the two spatial Holmboe modes. Conversely to the temporal case, the growth rates of the upstream and downstream modes differ (Ortiz *et al.* 2002). Our results show that at small Reynolds numbers the downstream mode grows, while the upstream mode remains stable. With the increase of the Reynolds number the upstream mode destabilizes and attains a significantly larger growth rate than the downstream one. Comparing the phase velocities of the two Holmboe modes in the reference frame moving with the mean velocity of the base flow we find that these absolute phase velocities are different. The difference tends to increase with the increase of the Richardson number.

In case of a viscous flow we also compute the critical values of the Reynolds number at which the temporal and spatial instabilities of the hyperbolic tangent velocity profile set in. We also study their dependence on the mixing layer thickness and the Richardson number. A similar problem was studied by Defina, Lanzoni & Susin (1999) for the flow in a tilted tube, but was not addressed before for the stratified mixing layer with tanh velocity and density profiles. In particular we show that the critical Reynolds number corresponding to the K-H instability is the same for both temporal and spatial instabilities.

Finally, following the findings of Smyth & Peltier (1990) and Haigh (1995), we study the possibility that the onset of Holmboe instability may take place as a three-dimensional oblique wave. It is found that, in complete agreement with the

predictions of Smyth & Peltier (1988, 1990), three-dimensional Holmboe modes become most unstable at large Richardson and low Reynolds numbers. We have found this three-dimensional instability not only for the temporal, but also for the spatial case.

In the following (§ 2) we formulate the spatial problem for the parametrically forced stratified mixing layer and define the temporal problem related to the spatial formulation. We propose a relatively simple iteration procedure, which yields the solution of the spatial stability problem. The first iteration of this procedure yields the solution of the temporal problem as well. Thus, the solutions of both problems can be compared just by comparison of results obtained at the first and the last iterations of the same iteration procedure. The results are described in the § 3. The description of results begins with a comparison of the temporal and spatial perturbation profiles and amplification rates. We continue by studying the dependence of the amplification rates, spatial periods and temporal frequencies of perturbations on the Reynolds and Richardson numbers, and the layer thickness. This is followed by a discussion of applicability of the Gaster transformation. Then we discuss the neutral stability curves calculated for the viscous mixing layer flow. Finally we discuss the possibility of primary three-dimensional instability onset. Conclusions are presented in the § 4.

## 2. Problem formulation and numerical methods

Consider the flow of a Boussinesq incompressible fluid in a thermally stratified mixing layer. The flow is described by the momentum, energy and continuity equations:

$$\left.\begin{aligned} &\frac{\partial \boldsymbol{v}}{\partial t} + (\boldsymbol{v}\cdot\nabla)\boldsymbol{v} = -\frac{1}{\rho}\nabla p + \nu\Delta\boldsymbol{v} + g\gamma(T-\bar{T})\boldsymbol{e}_y, \\ &\nabla\cdot\boldsymbol{v} = 0, \quad \frac{\partial T}{\partial t} + (\boldsymbol{v}\cdot\nabla)T = k\Delta T. \end{aligned}\right\} \tag{1}$$

Here $\boldsymbol{v}$, $p$ and $T$ are the fluid velocity, pressure and temperature, respectively; $\rho$ is the density, $\nu$ is the kinematic viscosity, $\gamma$ is the thermal expansion coefficient, $\kappa$ is the thermal diffusivity, $g$ is the gravitational acceleration, $\boldsymbol{e}_y$ is the unity vector in the $y$-direction and $\bar{T}$ is defined below.

### 2.1. *Spatial problem*

The spatial problem is defined in accordance with mixing layer experiments, e.g. Gaster *et al.* (1985), Weisbrot & Wygnansky (1988), Rajaee & Karlsson (1992), Hajj (1997), and Estevadeordal & Kleis (2002). These experiments can be described schematically as follows. Two fluid layers having different temperatures $T_1$ and $T_2$ and moving with different horizontal velocities $U_1$ and $U_2$ meet at a certain point, e.g. at the end of a splitter plate. A flapper or a loudspeaker introduces a time-periodic perturbation with a constant circular frequency $\omega_0$. This perturbation triggers the instability, which develops spatially in the streamwise direction.

We consider this problem in a domain $0 \leqslant x \leqslant \infty$, $-\infty \leqslant y \leqslant \infty$, $0 \leqslant z \leqslant 2\pi/\alpha_z$, where $\alpha_z$ is the spanwise wavenumber. The boundary conditions are

$$\text{at } y = -\infty: \qquad v_y = 0, \quad v_x = U_1, \quad T = T_1; \tag{2}$$

$$\text{at } y = +\infty: \qquad v_y = 0, \quad v_x = U_2, \quad T = T_2; \tag{3}$$

and periodicity conditions are implied in the $z$-direction. The initial velocity and temperature profiles are defined as

$$U_0(y) = U_1 + \tfrac{1}{2}(U_2 - U_1)[1 + f(y)], \tag{4}$$

$$T_0(y) = T_1 + \tfrac{1}{2}(T_2 - T_1)[1 + g(y)], \tag{5}$$

where functions $f(y)$ and $g(y)$ vary between $-1$ and 1 and describe initial velocity and temperature profiles, for example tanh or piecewise-linear profiles.

In the following we assume that the instability is excited with a harmonic perturbation of frequency $\omega_0$. To render the equations dimensionless we follow Gaster *et al.* (1985) and use the spatial wavelength of the exciting perturbation, i.e. $[L]=(U_1+U_2)/2\omega_0$, for definition of the length scale. The following scales are introduced for the velocity, time, pressure and temperature, respectively: $[v]=U_2-U_1$, $[t]=L/[v]$, $[p]=\rho[v]^2$, and $[T]=T_2-T_1$. The mean values of the velocity and the temperature are defined as $\overline{U}=(U_1+U_2)/2$ and $\overline{T}=(T_1+T_2)/2$. The scales are chosen in such a way that the dimensionless length over which the exciting perturbation is advected by the mean velocity $\overline{U}$ during one period of oscillation $\tau=2\pi/\omega_0$ is $x_\tau=\overline{U}\tau/[L]=2\pi$. This yields the spatial wavenumber of the exciting perturbation $\alpha_0=2\pi/x_\tau=1$. The length scale can also be expressed using the mean velocity or the velocity ratio $\lambda$ as $[L]=\overline{U}/\omega_0=[v]/2\lambda\omega_0$. Equations (1) in dimensionless form become

$$\left.\begin{aligned} &\frac{\partial \boldsymbol{v}}{\partial t}+(\boldsymbol{v}\cdot\nabla)\boldsymbol{v}=-\nabla p+\frac{1}{Re}\Delta\boldsymbol{v}+Ri(T-\overline{T})\boldsymbol{e}_y,\\ &\nabla\cdot\boldsymbol{v}=0,\quad \frac{\partial T}{\partial t}+(\boldsymbol{v}\cdot\nabla)T=\frac{1}{Pe}\Delta T, \end{aligned}\right\} \tag{6}$$

where $Re=[v][L]/\nu$ is the Reynolds number, $Pe=[v][L]/\kappa$ is the Péclet number and $Ri=g\gamma[T][L]/[v]^2$ is the bulk Richardson number. In the stability studies for the spatial problem we assume that the perturbations behave proportionally to $\exp[\mathrm{i}(\alpha x+\alpha_z z-\omega_0 t)]$ and look for the complex spatial wavenumber $\alpha$, which yields the fastest spatial growth of the perturbation having the fixed temporal frequency $\omega_0$. The dimensionless value of $\alpha_z$ plays the role of an additional governing parameter.

### 2.2. *Temporal problem*

For the temporal problem we consider two fluid layers moving at $y=\pm\infty$ with opposite velocities $U_{max}$ and $-U_{max}$ at $y=\pm\infty$. This problem is also described by equations (6), but is considered in a domain $0\leqslant x\leqslant X_t=2\pi/\alpha_0$, $-\infty\leqslant y\leqslant\infty$, $0\leqslant z\leqslant 2\pi/\alpha_z$ where $\alpha_0$ is the fixed spatial wavenumber of the temporal problem. The boundary conditions for the temporal problem are:

$$\text{at } y=-\infty: \qquad v_y=v_z=0,\quad v_x=-U_{max},\quad T=T_1; \tag{7}$$

$$\text{at } y=+\infty: \qquad v_y=v_z=0,\quad v_x=U_{max},\quad T=T_2; \tag{8}$$

and periodicity conditions in the horizontal direction:

$$\left.\begin{aligned} &\boldsymbol{v}(x=0)=\boldsymbol{v}(x=X_t),\ p(x=0)=p(x=X_t),\ T(x=0)=T(x=X_t),\\ &\left[\frac{\partial \boldsymbol{v}}{\partial x}\right]_{x=0}=\left[\frac{\partial \boldsymbol{v}}{\partial x}\right]_{x=X_t},\ \left[\frac{\partial p}{\partial x}\right]_{x=0}=\left[\frac{\partial p}{\partial x}\right]_{x=X_t},\ \left[\frac{\partial T}{\partial x}\right]_{x=0}=\left[\frac{\partial T}{\partial x}\right]_{x=X_t}. \end{aligned}\right\} \tag{9}$$

Similar periodicity conditions are posed in the $z$-direction. The initial velocity profile is defined as

$$U(y)=U_{max}f(y) \tag{10}$$

and the initial temperature profile is the same as for the spatial problem. The function $f(y)$ is the same as in (4).

Similarly to the spatial problem, we choose the length scale of the temporal problem such that its dimensionless wavelength becomes equal to $2\pi$. The following scales of length, velocity, time, pressure and temperature are chosen for the temporal problem: $[L]=\alpha_0^{-1}$, $[v]=2U_{max}$, $[t]=1/\alpha_0[v]$, $[p]=\rho[v]^2$, and $[T]=T_2-T_1$. Obviously, the

| | Spatial problem | Temporal problem |
|---|---|---|
| *Scales:* | | |
| $[L]$, length | $(U_2+U_1)/2\omega_0$ | $1/\alpha_0$ |
| $[v]$, velocity | $U_2-U_1$ | $2U_{max}$ |
| $[t]=[L]/[v]$, time | $L/(U_2-U_1)=1/2\lambda\omega_0$ | $L/2U_{max}=1/2\alpha_0U_{max}$ |
| $[p]=\rho[v]^2$, pressure | $\rho(U_2-U_1)^2$ | $4\rho U_{max}^2$ |
| $[T]$, temperature | $T_2-T_1$ | $T_2-T_1$ |
| *Governing parameters:* | | |
| Reynolds number, $Re=[v][L]/\nu$ | $(U_2-U_1)(U_2+U_1)/2\omega_0\nu$ | $2U_{max}/\alpha_0\nu$ |
| Richardson number, $Ri=g\beta[T][L]/[v]^2$ | $g\beta(T_2-T_1)/2(U_2-U_1)\omega_0\lambda$ | $g\beta(T_2-T_1)/4U_{max}^2\alpha_0$ |
| Péclet number, $Pe=[v][L]/\kappa$ | $(U_2-U_1)(U_2+U_1)/2\omega_0\kappa$ | $2U_{max}/\alpha_0\kappa$ |

TABLE 1. Scales and governing parameters chosen to render the temporal and spatial problems dimensionless. The perturbations are defined as $\exp[\mathrm{i}(\alpha x-\omega_0 t)]$ and $\exp[\mathrm{i}(\alpha_0 x-\omega t)]$ for the spatial and temporal problems, respectively, where $\omega_0$ and $\alpha_0$ are real and positive. The velocity ratio is defined as $\lambda=(U_2-U_1)/(U_2+U_1)$.

dimensionless temporal problem is also described by equations (6). Its dimensionless $x$-coordinate varies from zero to $2\pi$, so that the dimensionless spatial wavenumber is unity. The perturbation is assumed to be proportional to $\exp[\mathrm{i}(\alpha_0 x+\alpha_z z-\omega t)]$ and we look for the complex temporal amplification rate $\omega$, which yields the fastest temporal growth of the perturbation having the fixed $x$-wavenumber $\alpha_0$. As in the spatial formulation, the dimensionless value of the $z$-wavenumber $\alpha_z$ plays the role of an additional governing parameter.

The scales and governing parameters defined for the spatial and temporal problems are summarized in table 1. It follows that both problems are described by the same governing parameters if $U_{max}=(U_2-U_1)/2$ and $\alpha_0=2\omega_0/(U_1+U_2)$. Thus, we associate the spatial parametrically excited problem with the temporal problem whose spatial period coincides with $2\pi/\alpha_0$. The temperature profiles of the two problems must coincide and the velocity profiles must have the same velocity difference and be described by the same shape function $f(y)$.

### 2.3. *Linear stability problem*

Consider spatial and temporal problems that are associated as described above. Assume also that the parametrically excited spatial instability occurs with the dimensionless spatial wavenumber $\alpha_s$, which slightly diverges from unity (recall that $\alpha_0$ is exactly one). We observe the development of the instability (e.g. growth of a K-H billow in a mixing layer) in the reference frame moving with the mean velocity $\overline{U}$ and compare it with the instability developing in the temporal problem having the fixed spatial wavenumber exactly equal to one. We wish to study the difference between the spatial and temporal instabilities. Assuming that the spatial stability problem yields a complex value of $\alpha$, a measure of the difference between the wavenumbers of spatial and temporal instabilities will be the difference between the dimensionless value of $\mathrm{Re}(\alpha)$ and unity. We will also compare spatial and temporal amplification rates. This comparison will require a rescaling, which is defined below.

In the following we describe a simple iterative procedure which yields both spatial and temporal fastest growing perturbations, and a method to compare them. We assume that the basic flow is decribed by the same dimensionless temperature profile and by the dimensionless velocity profiles $U_s(y)$ and $U_t(y)$ for the spatial and the

temporal problems, respectively:

$$T(y)=\frac{T_1}{T_2-T_1}+\frac{1}{2}[1+g(y)],\quad U_S(y)=\frac{U_1}{U_2-U_1}+\frac{1}{2}[1+f(y)],\quad U_t(y)=\frac{1}{2}f(y). \tag{11}$$

The perturbations are defined as $A(y)\exp[\mathrm{i}(\alpha x+\alpha_z z+\omega t)]$, where $A(y)$ is the amplitude, and $\alpha$, $\omega$ and $\alpha_z$ are as defined above. For the spatial problem, we assume that $\alpha$ is complex and $\omega$ has a prescribed real value, while for the temporal problem $\alpha$ is real (according to our scaling $\alpha=1$) and $\omega$ is complex. Note that, according to the scales chosen for the spatial problem,

$$\omega=\omega_0[t]=\frac{1}{2}\frac{U_1+U_2}{U_1-U_2}=\frac{1}{2\lambda},\quad \text{where}\quad \lambda=\frac{U_1-U_2}{U_1+U_2}. \tag{12}$$

It is emphasized that (12) holds only for the spatial case. The new parameter $\lambda$ is zero when $U_1=U_2$ (no shear) and is infinite for the classical temporal case where $U_2=-U_1=U_{max}$. Note also that $\lambda<1$ corresponds to the cases where the two fluid layers of the spatial problem move in the same direction, while $\lambda>1$ means that the directions of motion are opposite.

The linearized stability problem for both spatial and temporal cases is described by the non-isothermal Orr–Sommerfeld equations ($w$ and $\theta$ are perturbations of the vertical velocity and the temperature respectively) as

$$\begin{aligned}-\mathrm{i}\omega(w''-a^2w)=\mathrm{i}\alpha[a^2U(y)w-U(y)w''+wU''(y)]\\ -\frac{1}{Re}\left[w^{(4)}-2a^2w''+a^4w\right]-Ria^2\theta,\end{aligned} \tag{13}$$

$$-\mathrm{i}\omega\theta=-[\mathrm{i}\alpha U(y)\theta+T'(y)w]+\frac{1}{Pe}[\theta''-a^2\theta], \tag{14}$$

with $a^2=\alpha^2+\alpha_z^2$ and the above assumptions for $\alpha$ and $\omega$. The profile $U(y)$ must be replaced by one of the profiles (11) depending on the problem considered.

### 2.4. *The iteration procedure*

We illustrate our approach for the case of inviscid and isothermal fluid. In this case eq. (13) reduces to the Rayleigh equation (assume $\alpha_z=0$)

$$\left[U(y)-\frac{\omega}{\alpha}\right](w''-\alpha^2w)-U''(y)w=0 \tag{15}$$

which can be considered as a linear eigenproblem for $\omega$ or a nonlinear eigenproblem for $\alpha$. For the temporal case $U=U_t(y)=f(y)$, $\alpha=\alpha_0=1$, and (15) becomes

$$\left[\tfrac{1}{2}f(y)-\omega\right](w''-w)-\tfrac{1}{2}f''(y)w=0. \tag{16}$$

For the spatial case we have to account for (12) and profile $U_s(y)$. We assume additionally that for the spatial case $\alpha=1+\beta$, where $\beta$ is a complex correction to the unity wavenumber of the exciting perturbation. Using (11) and (12) we note that $U_s(y)-\omega/\alpha=\beta/2\lambda(1+\beta)+f(y)/2)$, and (15) reduces to

$$\left[\frac{1}{2}f(y)+\frac{1}{2\lambda}\frac{\beta}{1+\beta}\right](w''-(1+\beta)^2w)-\frac{1}{2}f''(y)w=0. \tag{17}$$

Similarity of the equations (16) and (17) allows us to define the following iterative procedure:

$$\left[\frac{1}{2}f(y)+\frac{1}{2\lambda}\frac{\beta_{k+1}}{1+\beta_k}\right](w''_{k+1}-(1+\beta_k)^2w_{k+1})-\frac{1}{2}f''(y)w_{k+1}=0 \tag{18}$$

where $\beta_0 = 0$ and each successive $\beta_{k+1}$ is chosen as the leading eigenvalue of the $(k+1)$th eigenvalue problem (18). Note that the eigenvalue problem is linear with respect to $\beta_{k+1}$, so that standard methods for linear eigenproblems can be applied at each iteration. Apparently, the converged iterative process yields the spatial amplification rate, $\alpha_i = \beta_i$, the spatial wavenumber $\alpha_r = 1 + \beta_r$ and the eigenvector of the spatial stability problem. Furthermore, comparison of equation (18) for $\beta_1$ and (16) shows that the first iteration yields the eigenvalue of the temporal problem, i.e.

$$\omega = -\beta_1/2\lambda \tag{19}$$

as well as the corresponding eigenvector.

It can be easily shown that for the general three-dimensional case taking into account also viscosity, heat conduction, and stratification, a similar iterative process can be constructed. The resulting equations are

$$\left[\frac{1}{\lambda}\frac{\beta_{k+1}}{1+\beta_k} + f(y)\right]\left(w''_{k+1} - a_k^2 w_{k+1}\right) = f''(y)w_{k+1} - \frac{2\mathrm{i}}{Re\,(1+\beta_k)}\left[w^{(4)}_{k+1} - 2a_k^2 w''_{k+1} + a_k^4 w_{k+1}\right] + 2\mathrm{i}Ri\,\frac{a_k^2}{(1+\beta_k)}\theta_{k+1}, \tag{20}$$

$$\left[\frac{1}{\lambda}\frac{\beta_{k+1}}{1+\beta_k} + f(y)\right]\theta_{k+1} = \frac{2\mathrm{i}}{1+\beta_k}T'(y)\,w - \frac{2\mathrm{i}}{Pe\,(1+\beta_k)}\left[\theta''_{k+1} + a_k^2\theta_{k+1}\right], \tag{21}$$

where $a_k^2 = (1+\beta_k)^2 + \alpha_z^2$ and (19) holds for the temporal case.

The proposed iterative procedure yields solutions for both the temporal and the spatial stability problems, which are linked by taking their length and velocity scales to be equal as described above. Using the iterations (20), (21) we can compare the eigenvectors of the two problems. The dimensionless temporal and spatial amplification rates can also be compared via (19). In fact, it is necessary to compare values of $\beta_1$ and the converged $\beta$. Furthermore, since at the converged value of $\beta$ it is possible to control the whole spectrum of the spatial problem, including the fastest growing mode, it is possible to calculate the critical values of the Richardson and Reynolds numbers corresponding to $\mathrm{Im}(\beta) = 0$.

Recall that according to the chosen time scale and (12) $\omega_0 = 0.5(U_1 + U_2)/(U_1 - U_2)$, i.e. the dimensionless frequency of the excitation is equal to the dimensionless mean velocity $\overline{U}$. Taking into account that the phase velocity of a perturbation is $v_f = \mathrm{Re}[\omega_0/(1+\beta)]$ we can distinguish between perturbation modes with $v_f > -\overline{U}$, which propagate downstream with respect to the mean velocity of the basic flow, and the modes with $v_f < \overline{U}$ which propagate upstream. The results on spatial instability reported below show that, as a rule, $v_f \neq \overline{U}$.

### 2.5. *Numerical methods*

Equations (20) and (21) are solved by two independent numerical approaches. The first one is based on centred finite differences, employing stretching of the grid where necessary. The second method is based on the global Galerkin technique with the basis functions constructed as linear superpositions of Chebyshev polynomials that analytically satisfy all the boundary conditions (Gelfgat 2001). The two methods are employed to cross-validate each other.

The application of the global Galerkin method requires decomposition of the basic flow profiles $U(y)$ and $T(y)$ in series of Chebyshev polynomials. In the case of hyperbolic tangent profiles ($\sim \tanh(y/\xi)$, see below) the convergence of these series appears to be rather slow, especially for values of $\xi$ below 0.1. For this reason the

majority of the results described below have been obtained using the finite difference method with the number of nodes varying between 500 and 2000. The computational domain was defined as an interval $-W \leqslant y \leqslant W$. The value of $W$ is chosen to ensure the independence of the results of further increase of its value, which sometimes requires $W$ of the order of $100\xi$. The grid was stretched near the centreline $y=0$ using the function $\tanh(sy/W)/\tanh(s)$, where $s$ was varied between 2 and 4 depending the value of $\xi$.

The boundary conditions for the mixing layer problem are defined using the asymptotic behaviour of the perturbations at $y \to \pm\infty$, as described in Michalke (1965) and Lie & Riahi (1988).

To validate the codes we carried out the following comparisons with independent results. First, we considered the Rayleigh equation (15) and reproduced the results of Michalke (1965) on spatial instability of an inviscid mixing layer flow. Our results obtained on the 300-node grid coincide with those of reported in table 1 of Michalke (1965) to within the fourth decimal digit. Then, to validate the inviscid stratified case we use the result of Smyth & Peltier (1989). For the gradient Richardson number $J=0.6$, $R=3$ (defined in § 3) and the spatial period scaled by the velocity layer depth $\alpha/\delta=0.3$ they reported the phase speed of the Holmboe wave $c=0.505467-$ i0.083320. Our result obtained for the 1000-node grid with $s=3$ is $c=0.505486-$ i0.0833. To validate the viscous term we reproduced the critical Reynolds number corresponding to the two-dimensional linear instability of the plane Poiseuille flow (our converged result is $Re_{cr}=5772.2414$, $\alpha_{cr}=1.022725$, $\omega_{cr}=0.2702383$) and the linear stability results for the stratified mixing layer published recently by Hogg & Ivey (2003) (their figure 4). Additionally, we monitored the convergence of both numerical methods and for several control cases checked that both methods yield same results.

## 3. Results

We consider a mixing layer flow with hyperbolic tangent velocity profiles. Assuming that the thicknesses of the velocity and temperature layers are $\delta$ and $\delta_t$, respectively, the basic profiles are defined by

$$f(y)=\tanh\left(\frac{y}{\xi}\right), \quad g(y)=\tanh\left(\frac{y}{\xi_t}\right) \tag{22}$$

where the coordinate $y$ is dimensionless, $\xi$ and $\xi_t$ are the dimensionless thicknesses $\delta$ and $\delta_t$ scaled by the length scales introduced above. The different thicknesses of the velocity and temperature layers define an additional governing parameter $R=\delta/\delta_t=\xi/\xi_t$. Based on the Miles–Howard semicircle theorem (Miles 1961; Howard 1961) Hazel (1972) showed that an instability of an inviscid stratified mixing layer can be expected for $R>2$. For the non-isothermal case considered here we use the fixed values of the Prandtl and $R$ numbers, $Pr=9$ and $R=3$, which approximately correspond to $\delta$ and $\delta_t$ of stratified water.

Note that if, according to a traditional scaling, the thickness of the velocity layer $\delta$ is chosen as the length scale, then the ratio between the two scales is given by $\delta/[L]=\xi$. It is easy to see that the dimensionless parameter $\xi$ is equal to the wavenumber of the temporal problem $\alpha_t$ scaled by $1/\delta$: $\xi=\delta/(1/\alpha_t)=\alpha_t/(1/\delta)$ . It is emphasized also that we describe our stability results in terms of $\beta_1$ and $\beta$, and not $\alpha$ and $\omega$. Such a description allows us to compare directly the temporal and the spatial problems. Thus, for example, the spatial and temporal instabilities correspond to $\mathrm{Im}(\beta)<0$ and

$\mathrm{Im}(\beta_1) < 0$, respectively. The values of $\alpha$ and $\omega$ can be recalculated as $\alpha = 1 + \beta$, and $\omega = -\beta_1/2\lambda$.

Following Hazel (1972) we calculate a gradient Richardson number $J$ corresponding to the profiles (22) and express it as a function of $Ri$, $R$, $\xi$, and $y$. For the temporal case this yields

$$J = -g\frac{\rho'(y)}{\rho_0}\frac{\delta}{[U'(y)]^2} = \frac{R\beta(T_2 - T_1)g}{2U_{max}^2\alpha_0}\frac{\xi^2\cosh^4(y/\xi)}{\cosh^2(Ry/\xi)} = 2Ri\,R\xi^2\frac{\cosh^4(y/\xi)}{\cosh^2(Ry/\xi)} \tag{23}$$

which at large $y$ can be approximated as

$$J = 2Ri\,R\xi^2\exp\left[2\frac{y}{\xi}(2 - R)\right]. \tag{24}$$

This means that if $R > 2$ (i.e. the result of Hazel 1972) we can always choose $y$ large enough to satisfy the condition of the Miles–Howard theorem $J < 1/4$. Therefore, for the tanh-profiles we expect to observe instabilities at significantly large Richardson numbers. Also Ortiz *et al.* (2002) noticed that in inviscid fluid with a piecewise linear velocity profile and stepwise density profile the Holmboe instability never vanishes with the increase of the bulk Richardson number. On the other hand, and according to the result of Hazel (1972), at $R < 2$ the Holmboe instability is not expected. This conclusion is supported by the experimental observations of Zhu & Lawrence (2001).

The value of the velocity ratio $\lambda$ was varied in the interval $0 < \lambda \leqslant 1$. As mentioned above, $\lambda > 1$ means that the two flows of the spatial case move in opposite directions. It is unclear how such a system might be realized experimentally. On the other hand, the iterative procedure (20) and (21) can be applied to larger values of $\lambda$. To check this point we performed a series of calculations up to $\lambda = 5$ (not shown here).

Since the Squire transformation always holds (Yih 1955; Koppel 1966) and, as explained by Smyth *et al.* (1988), the three-dimensional primary instability is a quite exceptional case, in most of the computations we set $\alpha_z = 0$. Non-zero values of $\alpha_z$ are considered in § 3.5.

### 3.1. *Isothermal inviscid flow*

In this case we solve the Rayleigh equation (15) using the iterative procedure (18). According to Drazin (1958), unstable temporal modes of (15) exist for $0 < \alpha\ \delta < 1$. These modes correspond to the K-H instability with $\omega = 0$. This implies that in the present formulation the unstable K-H modes exist for $0 < \xi < 1$. For $\xi \geqslant 1$ all the eigenmodes are neutral. Since equations (16) and (17) coincide for $\omega = \beta = 0$, all the eigenmodes of the spatial problem are also neutral for $\xi \geqslant 1$.

Figure 1 illustrates profiles of the streamwise velocity perturbation for different values of $\xi$ at $\lambda = 1$. The values of $\beta_1$ and the converged $\beta$ are shown below the corresponding frames. It is seen that the spatial (solid lines) and temporal (dashed lines) perturbation patterns are similar. The amplitudes of temporal perturbations are symmetric with respect to the axis $y = 0$, and their phases possess rotational symmetry around their value at $y = 0$. Clearly, these symmetries reflect the symmetry of the temporal problem and disappear in the spatial case (cf. dashed and solid lines in figure 1). This is the main qualitative difference between the temporal and spatial perturbation patterns. Our results show that at relatively small velocity ratio, e.g. $\lambda = 0.5$, the dimensionless spatial and temporal amplification rates rescaled by $\lambda$ (as in (19)) differ only by a few per cent. For $\lambda = 1$, however, this difference exceeds 35 % at $\xi = 0.2$ and is even larger at smaller values of $\xi$.

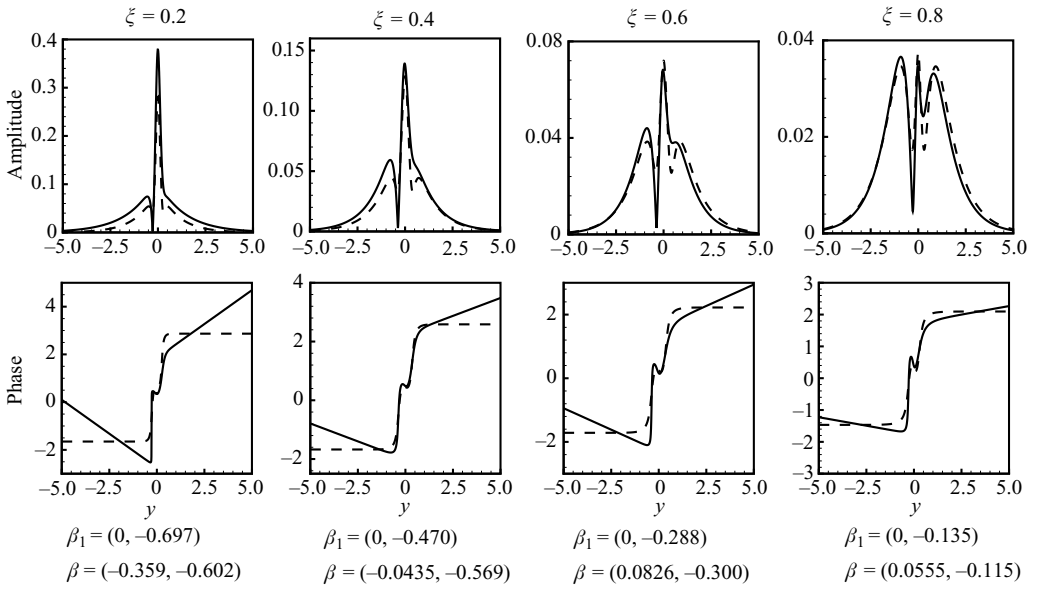


FIGURE 1. Amplitudes and phases of the temporal (dashed lines) and spatial (solid lines) perturbation of $x$-component of velocity for inviscid isothermal mixing layer flow. $\lambda = 1$.

The difference between the temporal and spatial instabilities for this case is summarized in figures 2($a$) and 2($b$), where $\beta_1$ (temporal instability) and converged $\beta$ (spatial instability) are shown as functions of $\xi$ for different $\lambda$. Only real parts of $\beta$ are included in figure 2($b$) since in the temporal case the K-H instability is monotonic and $\mathrm{Re}(\beta_1) = 0$. The temporal case is independent of $\lambda$, so that $\beta_1/\lambda$ remains constant. Thus, to compare spatial cases characterized by different $\lambda$ with the temporal case we report values of $\mathrm{Im}(\beta)/\lambda$ in figure 2($a$).

In the spatial and temporal cases the imaginary parts of $\beta_1$ and $\beta$ are close for $\lambda \leqslant 0.5$ (figure 2$a$). When $\lambda$ approaches unity the difference between them becomes noticeable at small $\xi$, and the dependence $\beta(\xi)$ for the spatial case becomes non-monotonic. Note that $\lambda = 1$ corresponds to $U_{min} = 0$, i.e. a motionless lower fluid layer. The obtained dependence of the amplification rate on the parameter $\lambda$ shows that the temporal and spatial instabilities are similar when the two layers move with similar velocities and become different when the velocities diverge.

### 3.2. *Isothermal viscous flow*

Viscous flow differs qualitatively from inviscid flow, since the neutral perturbation modes characteristic of the inviscid fluid turn out to be decaying at any viscosity. Apparently, at sufficiently large viscosity (sufficiently small Reynolds number) the flow is stable. The critical values of parameters are discussed in § 3.6. Here we are only interested in the effect of viscosity on the parameters $\beta_1$ and $\beta$, and on the profiles of the most unstable perturbations.

The same calculations as in the § 3.1 were repeated for isothermal viscous fluid at $Re = 100$. This value of the Reynolds number is beyond the critical value (see below), but is small enough to illustrate the influence of viscosity. The calculated values of $\beta_1$ and $\beta$ are reported in figures 2($c$) and 2($d$). As expected, the amplification rates of perturbations in the viscous fluids are smaller. The range of the layer thickness for which the instability is observed is also smaller, so that for $\xi > 0.9$ all the perturbations decay. The difference between the temporal and spatial wavenumbers also decreases.

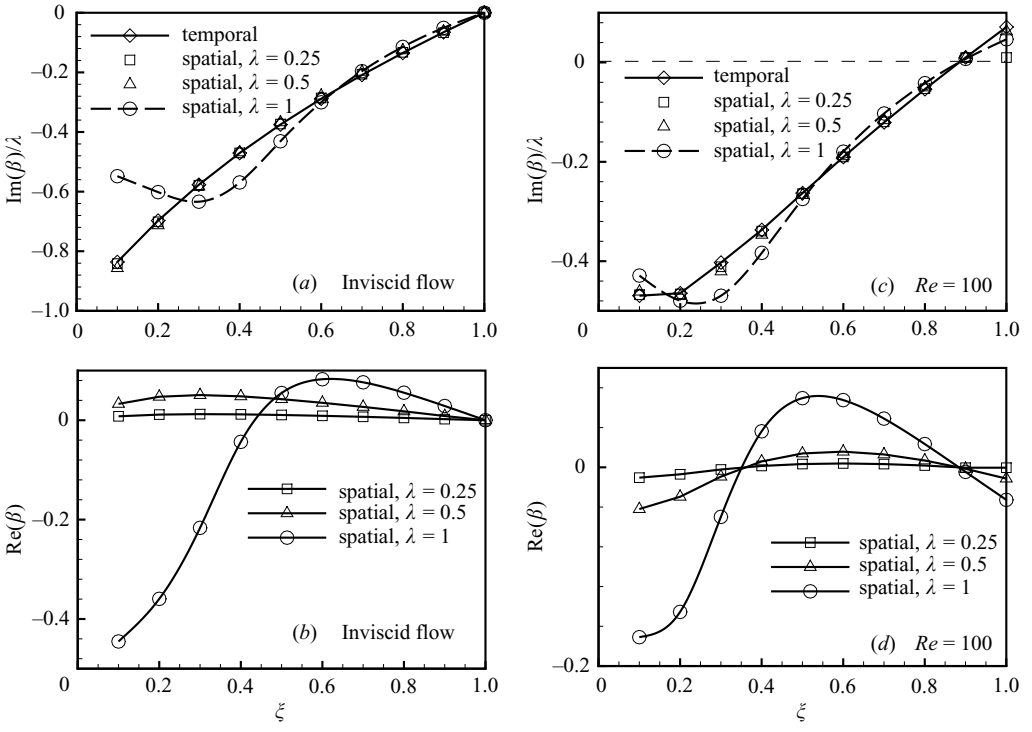


FIGURE 2. Dependence of the parameter $\beta$ on the dimensionless thickness of the velocity layer, $\alpha_z = 0$.

Wilson & Demuren (1996) studied how the spatial growth rate varies with the excitation frequency $\omega_0$ for a fixed mixing layer thickness. Using the definition of $\xi$, i.e. $\xi = 2\delta\omega_0/(U_1 + U_2)$, figures 3(*a*) and 3(*b*) can be easily transformed into the dependences $\alpha_i(\omega_0)$, from which a qualitative agreement with the result of Wilson & Demuren (1996) becomes obvious.

The profiles of the $x$-velocity perturbations are shown in figure 3 for $\lambda = 1$, the value for which we observe the largest differences between the inviscid and viscous cases, as well as between the temporal and spatial perturbations. Comparison of figures 1 and 3 shows that the inviscid and viscous perturbations have similar profiles for $\xi \leqslant 0.6$. The profiles become significantly different at $\xi = 0.8$.

### 3.3. *Effect of stratification: inviscid flows*

It is well-known that in a stratified mixing layer, together with the K-H instability there also exists a so-called Holmboe instability (Holmboe 1962). In the temporal case the Holmboe instability sets in through a pair of conjugate eigenvalues with $\mathrm{Re}(\omega) \neq 0$ and corresponds to the appearance of two waves travelling in opposite directions. Transitions between the two instabilities for the temporal case for inviscid fluid with heat conduction neglected were studied by Smyth & Peltier (1989). Here we show how the transition takes place in both the temporal and spatial cases and study the effect of both viscosity and heat conduction.

Figures 4 and 5 illustrate the transition between the K-H and Holmboe instabilities for the temporal and spatial cases, respectively, for inviscid fluid with heat conduction neglected. The calculations were carried out for $Ri = 0.2$, $R = 3$ and $\lambda = 0.5$. In the temporal case (figure 4) we observe a single steady K-H mode when the mixing layer is thin ($\xi < 0.2$). This mode is shown by triangles and a dash-and-dot line. Another

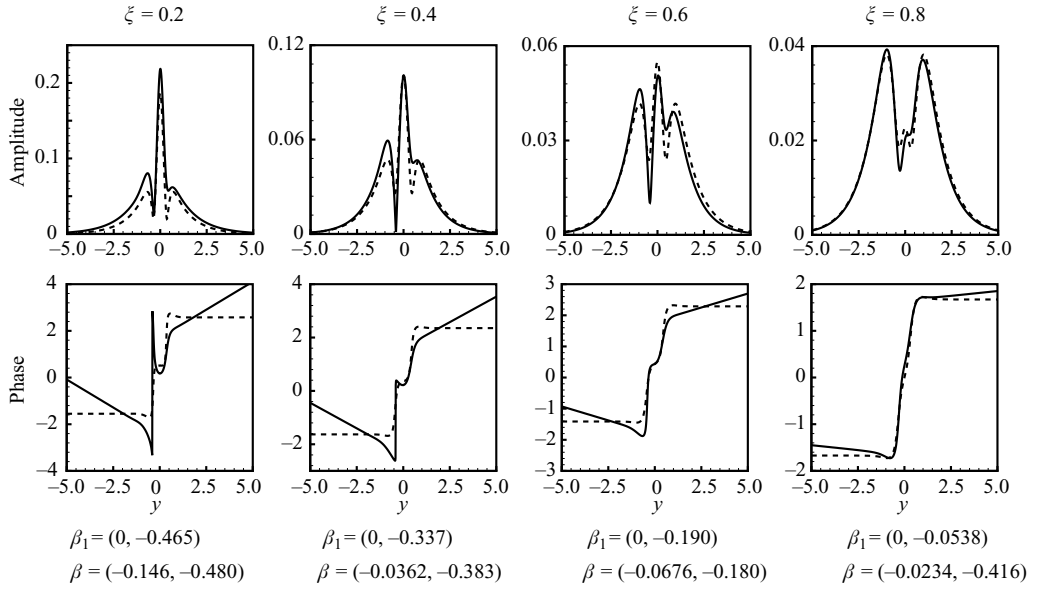


FIGURE 3. Amplitudes and phases of the temporal (dashed lines) and spatial (solid lines) perturbation of $x$-component of velocity for viscous isothermal mixing layer flow. $\lambda = 1$, $Re = 100$, $\alpha_z = 0$.

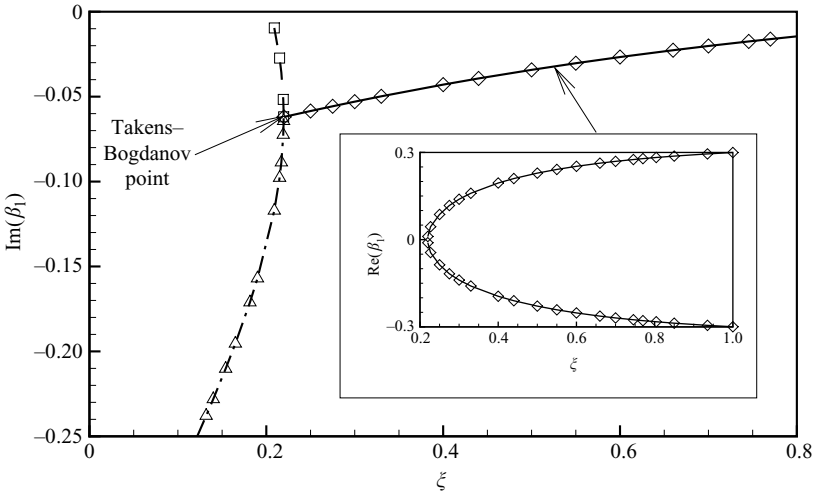


FIGURE 4. Dependence of the time amplification rate $\mathrm{Im}(\beta_1)$ on the depth of velocity layer $\xi$. Inviscid non-isothermal fluid flow, $Ri = 0.2$, $R = 3$, $\lambda = 0.5$, $\alpha_z = 0$. $\Delta$, first K-H mode; $\square$, second K-H mode; $\diamond$, Holmboe modes. The inset shows the dependence of $\mathrm{Re}(\beta_1)$ on $\xi$ for the two Holmboe modes.

steady K-H mode appears when the dimensionless thickness $\xi$ exceeds 0.2 (squares and a dashed line in figure 4). These two steady modes merge at $\xi = 0.2196$ and do not exist beyond this point. Two oscillatory modes (diamonds and a solid line in figure 4) appear at the point of merging, so that at larger $\xi$ only these oscillatory modes exist. The real parts of parameter $\beta_1$ (or real parts of $\omega$ in (19)) of these two modes are non-zero and have opposite signs, which is illustrated in the inset of figure 4. This is a clear sign of the Holmboe instability. Thus, we observe the replacement of

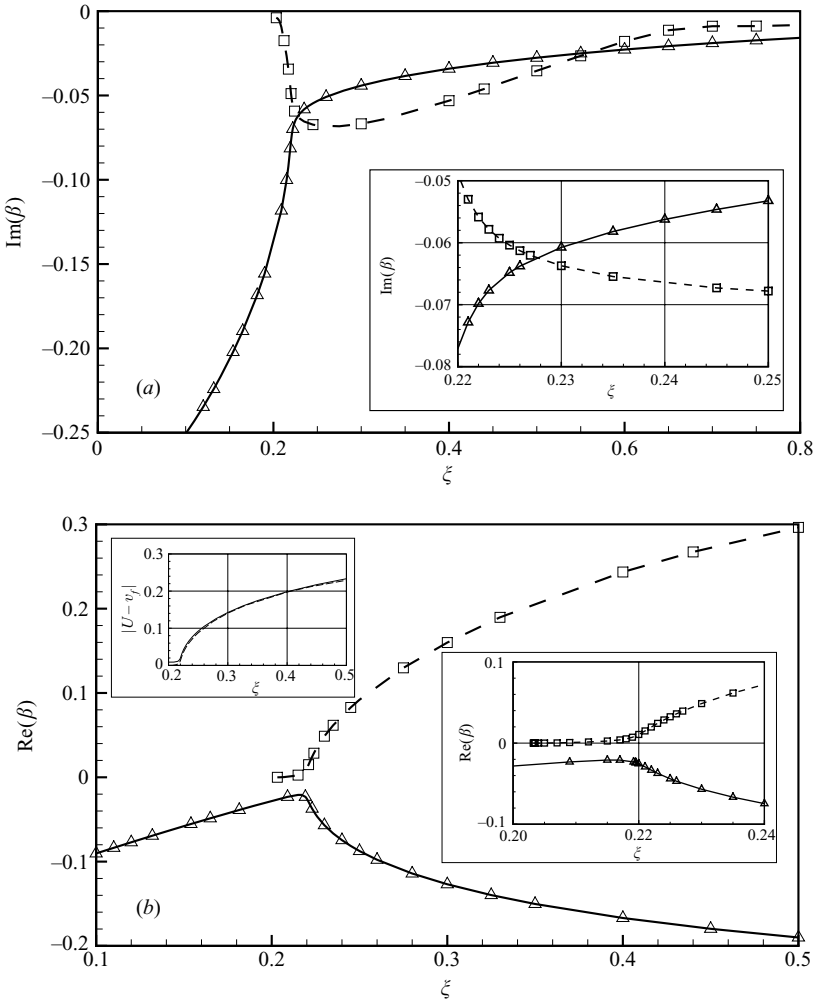


FIGURE 5. Dependence of parameter $\beta$ on the depth of velocity layer $\xi$ for the spatial instability. Inviscid non-isothermal fluid flow, $Ri = 0.2$, $R = 3$, $\lambda = 0.5$, $\alpha_z = 0$. $\Delta$, first K-H–Holmboe mode; $\square$, second K-H–Holmboe mode. The insets zoom in on the transitions from K-H to Holmboe type of instability. An additional inset in (*b*) shows the absolute difference between the phase velocity of Holmboe modes and average velocity of the base flow.

two steady K-H modes by two conjugated oscillatory Holmboe modes, which is a well-known Takens–Bogdanov codimension-two bifurcation point (Kuznetsov 2004). Smyth & Peltier (1989) obtained similar results for other values of $R$ and $Ri$. An analytical dispersion relation obtained for a stepwise density profile contains a similar bifurcation point (Lawrence, Broward & Redekopp 1991; Caulfield 1994; Haigh & Lawrence 1999; Ortiz *et al.* 2002 and references therein). The origin of the Takens–Bogdanov point in this dispersion relation is quite obvious and corresponds to a square root the argument of which changes its sign. Our results show that this point is also retained for continuous velocity and density profiles and for the complete model that accounts for viscosity and diffusion (see below).

In the spatial case the transition between the K-H and Holmboe modes is qualitatively different (figure 5). In this case we also observe a single K-H mode

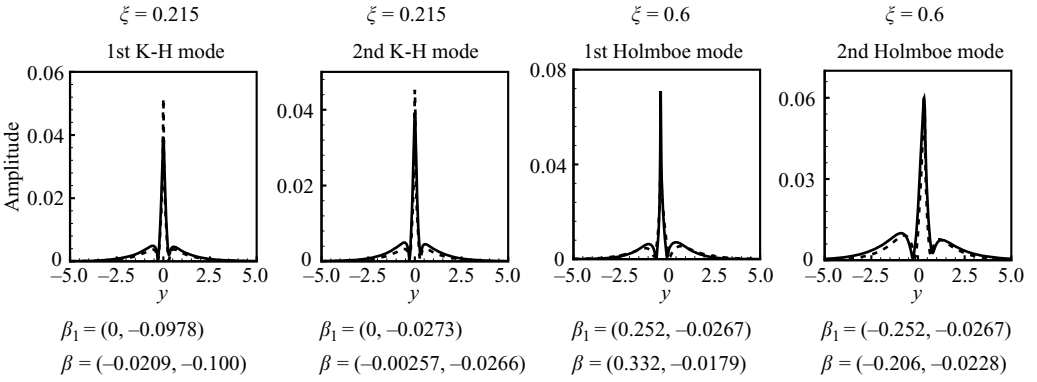


FIGURE 6. Amplitudes of the temporal (dashed lines) and spatial (solid lines) perturbations of $x$-component of velocity for inviscid stratified mixing layer flow. $\lambda = 0.5$, $Ri = 0.2$, $R = 3$, $\alpha_z = 0$.

for $\xi < 0.2$ shown by triangles and a solid line. Another unstable mode appears when the thickness $\xi$ exceeds 0.2, similarly to the temporal case (squares and dashed line in figure 5). When the second mode appears its value of $\mathrm{Re}(\beta)$ is small, which indicates that this is another K-H mode. At a certain value of $\xi$, which is close to the Takens–Bogdanov point of the temporal case, the real parts of $\beta$ for both modes start to grow rapidly (figure 5*b*). However, we observe a continuous change of each mode rather than an abrupt switch from one (K-H) mode to another (Holmboe). The latter is illustrated in the insets of figure 5, in which the area of the rapid growth of $\mathrm{Re}(\beta)$ is enlarged. For $\xi > 0.22$ we observe two unstable modes with large $\mathrm{Re}(\beta)$, which apparently correspond to the two Holmboe modes of the temporal case. Thus, conversely to the temporal problem, in the spatial case the K-H and Holmboe modes continuously transform one into the other.

As mentioned above, the two Holmboe waves propagate upstream and downstream with respect to the mean velocity of the base flow $\bar{U}$. To compare the phase velocity of the two modes in the reference frame moving with the mean velocity $\bar{U}$ we define the absolute phase velocity as $u_f = |\bar{U} - v_f|$. Taking into account the definition of the phase velocity $v_f = \mathrm{Re}(\omega_0/\alpha)$ it is easy to see that

$$u_f = \frac{1}{2\lambda}\left|\mathrm{Re}\left[\frac{\beta}{1+\beta}\right]\right|. \tag{25}$$

An additional inset in figure 5(*b*) shows $u_f$ of the two Holmboe modes. It is seen that although the velocities are very close, they do not coincide. This is in a qualitative agreement with the results of Ortiz *et al.* (2002) obtained for piecewise velocity and stepwise density profiles.

An additional illustration of the similarity of the spatial and temporal modes is shown in figure 6, where temporal and spatial perturbations corresponding to two K-H modes at $\xi = 0.215$ and two Holmboe modes at $\xi = 0.6$ are compared. The amplitude profiles, as well as the values of $\beta_1$ and $\beta$ of the corresponding temporal and spatial K-H perturbations are close at $\xi = 0.215$. In the case of Holmboe instability ($\xi = 0.6$) profiles of perturbations remain similar; however the difference in the values of $\beta_1$ and $\beta$ is more pronounced. Note that although the profiles of the Holmboe modes are shifted with respect to the centreline $y = 0$, they retain the shape of the K-H modes. Values of $\mathrm{Re}(\beta)$ show that the difference between the spatial periods of the temporal and spatial cases is small for the K-H instability. However, this difference

will be significantly increased in the wavelength of the Holmboe instability, for which $\mathrm{Re}(\beta)$ reaches the value of 0.5 (figures 5 and 6).

On studying the transition from the K-H to the Holmboe instability we observe two important facts. First, the perturbation profiles (figure 6) of both instabilities have similar shapes and differ mainly by the location of the maximum: at the midplane for K-H instability and above and below the midplane for the Holmboe instability. The location of the maximum yields a criterion to distinguish between the spatial K-H and Holmboe modes. Another criterion is the deviation of the phase velocity $v_f$ from the mean velocity $\bar{U}$; however it can be applied only far from the transition region. The second fact is that the spatial K-H and Holmboe modes continuously transform one into the other. Apparently, both instabilities are driven by an interplay of destabilizing shear and stabilizing buoyancy forces. A different ratio of these factors leads to either K-H or Holmboe instability that continuously transform one into the other. It would thus be natural to assume that the main driving mechanisms of both instabilities are the same, but depending on the ratio between shear and buoyancy the instability develops as a K-H or a Holmboe wave. Therefore, the explanations of the physics of instability for non-stratified (e.g. Batchelor 1967; Drazin & Reid 1984) and for stratified shear flow (e.g. Holmboe 1962; Baines & Mitsudera 1994; Caulfield 1994) must continuously transform one into another. Indeed, if it is assumed that the mechanism changes abruptly then an abrupt change of the leading eigenvalue and the perturbation profile would be observed, which does not happen. Therefore, we conclude that both K-H and Holmboe instabilities are driven by the same physical mechanism. Baines & Mitsudera (1994) arrived at a similar conclusion: "We emphasize that all of the instabilities described above may be interpreted in terms of one mechanism alone, namely the mutual forcing of two stationary, otherwise free, waves. This suggests that shear instability in general is due to this single mechanism, rather than a family of different processes".

The maximum of the perturbation profile of the K-H mode is always located at the plane where inflection point occurs. Assuming that the layer is stably stratified with the tanh-profile (22) we introduce the stabilizing buoyancy force. The location of its maximum coincides with the maximum of the density gradient, i.e. is also located at the plane $y=0$. When the stratification is large enough the maximum of the perturbation profile shifts towards the area where the density gradient is small while the shear still is large. The temporal velocity profile is antisymmetric with respect to the plane $y=0$, and the instability appears due to two symmetric shifts above and below the interface as two antisymmetric waves travelling in the opposite directions. In the spatial case the symmetry is broken, which leads to different growth rates and phase velocities of the two traveling waves. It is clear also why the width of the density layer must be smaller than that of the velocity layer: only in this case can the maximum of the perturbation profile be shifted into the region where the density gradient is small while the shear is still large. The maximal values of perturbations shown in figure 6 for $\xi=0.6$ are located at $y\approx\pm 0.327$. The gradient Richardson number (23) calculated at this location is $J\approx 0.11$, which is significantly below the value of 0.25.

### 3.4. *Effect of stratification: viscous flows*

Figures 7–9 illustrate the effect of viscosity on the transition between K-H and Holmboe instabilities. Figure 7 corresponds to the temporal and figures 8 and 9 to the spatial cases. At $Re=10^4$ (figures 7*a* and 8), when the viscosity is small, the transitions are similar to those observed for inviscid fluid. With the increase of

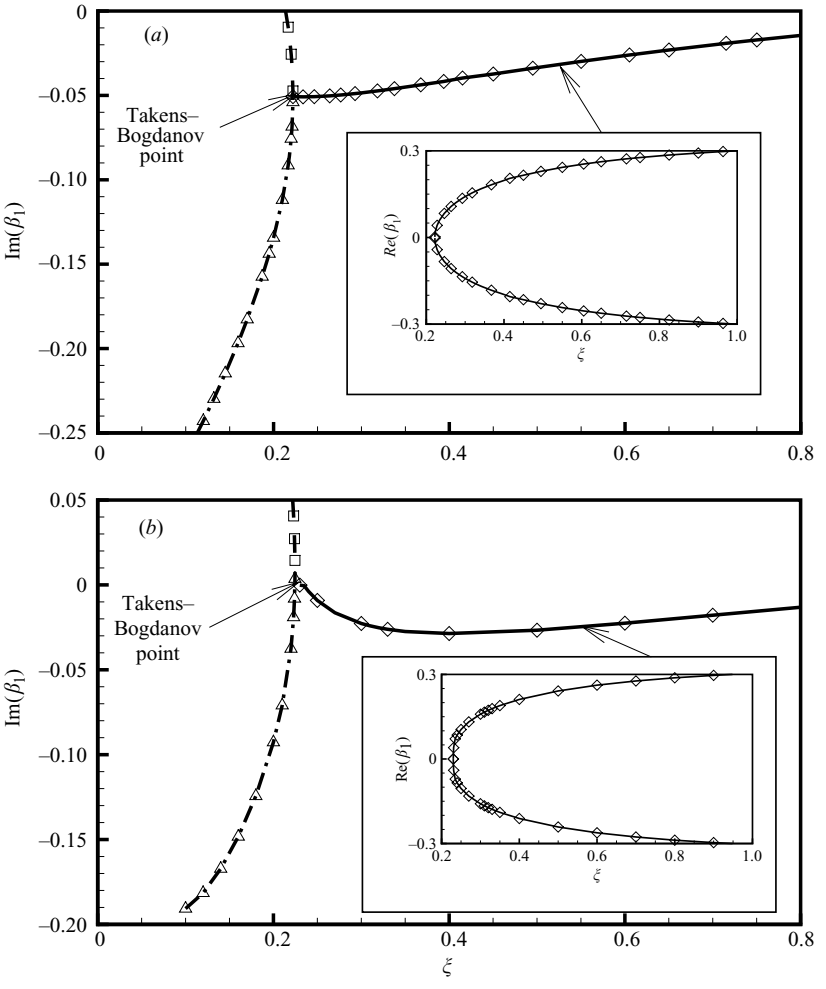


FIGURE 7. Dependence of the time amplification rate $\mathrm{Im}(\beta_1)$ on the depth of velocity layer $\xi$. Viscous non-isothermal flow. $Ri = 0.2$, $Pr = 9$, $R = 3$, $\lambda = 0.5$, $\alpha_z = 0$. (*a*) $Re = 10^4$, (*b*) $Re = 10^3$. $\Delta$, first K-H mode; $\square$, second KH mode; $\diamond$, Holmboe modes. The insets show the dependence of $\mathrm{Re}(\beta_1)$ on $\xi$ for the two Holmboe modes.

viscosity and the corresponding decrease of the Reynolds number ($Re = 10^3$, figures 7*b* and 9) the temporal and spatial amplification rates decrease, as expected. The Takens–Bogdanov point (figure 7*b*) shifts into the region of decaying perturbations corresponding to $\mathrm{Im}(\beta) > 0$. However, the transitions remain qualitatively the same. Note that in such case the two instabilities arise in separate intervals of $\xi$: the K-H modes are unstable for $\xi \leqslant 0.224$, while the Holmboe modes are unstable for $\xi \geqslant 0.23$. With further increase of viscosity the distance between the two intervals appears to increase. A laboratory or direct numerical simulation of such cases would reveal two instabilities setting in at different layer thicknesses, so that the K-H instability will decay at a certain layer thickness, while the Holmboe instability will start at a larger thickness. In this case the continuous transition between the K-H and Holmboe instabilities could be overlooked and incorrect conclusions drawn.

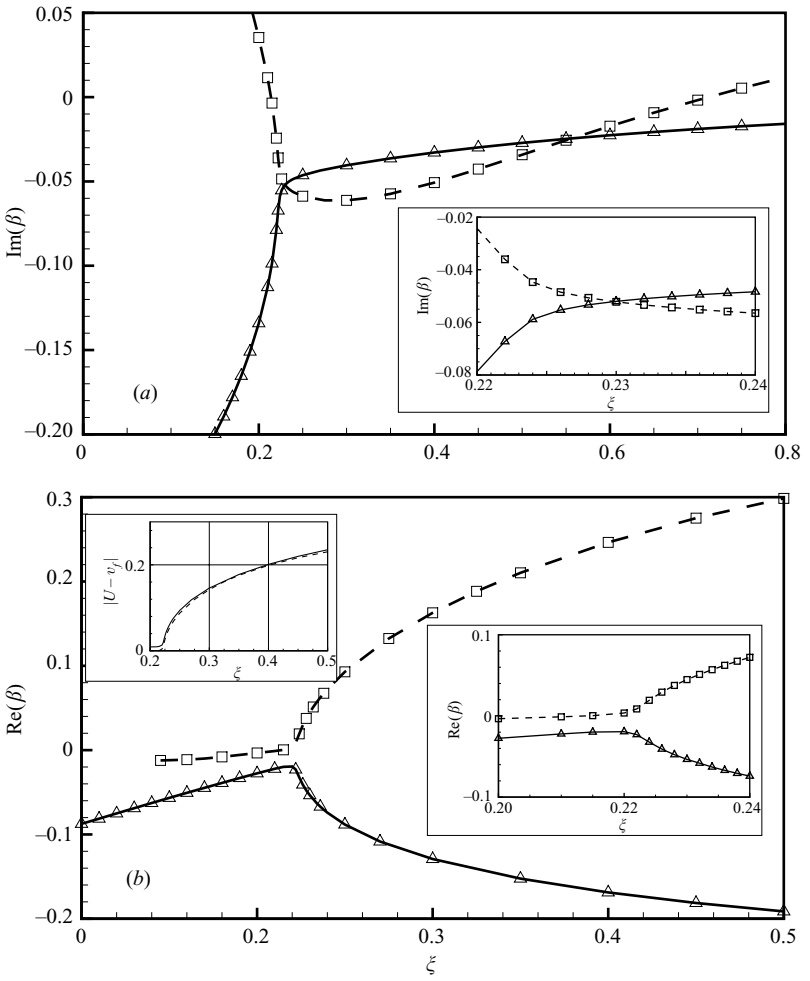


FIGURE 8. Dependence of parameter $\beta$ on the depth of velocity layer $\xi$ for the spatial instability. Viscous non-isothermal flow, $Re = 10^4$, $Ri = 0.2$, $Pr = 9$, $R = 3$, $\lambda = 0.5$, $\alpha_z = 0$. $\Delta$, first K-H–Holmboe mode; $\square$, second K-H–Holmboe mode. The insets zoom in on the transitions from K-H to Holmboe type of instability. An additional inset in frame (*b*) shows the absolute difference between the phase velocity of Holmboe modes and average velocity of the base flow.

At relatively large viscosity (small Reynolds number) the behaviour of one of the spatial modes changes qualitatively (figure 9). The imaginary part of $\beta$ of the mode shown by the solid line does not grow monotonically, as it did in the cases of inviscid and low-viscosity fluids, but rather changes abruptly at the point of the K-H–Holmboe transition. Comparison with the temporal case (figure 7*b*) shows that this abrupt change is a reflection of the sharp angle at which the temporal Holmboe mode is attached to the merging K-H modes. Note also that the difference between the absolute phase velocities (insets in figures 8*b* and 9*b*) remains rather small and is slightly larger at smaller Reynolds number.

Figures 10 and 11 show how the parameter $\beta$ depends on the Richardson number for inviscid and viscous fluids, when the thickness of the mixing layer is constant. Considering the temporal instability, the Takens–Bogdanov points also exist in the plane Im($\beta$)–*Ri* (figure 10). The transition between the K-H and the Holmboe modes

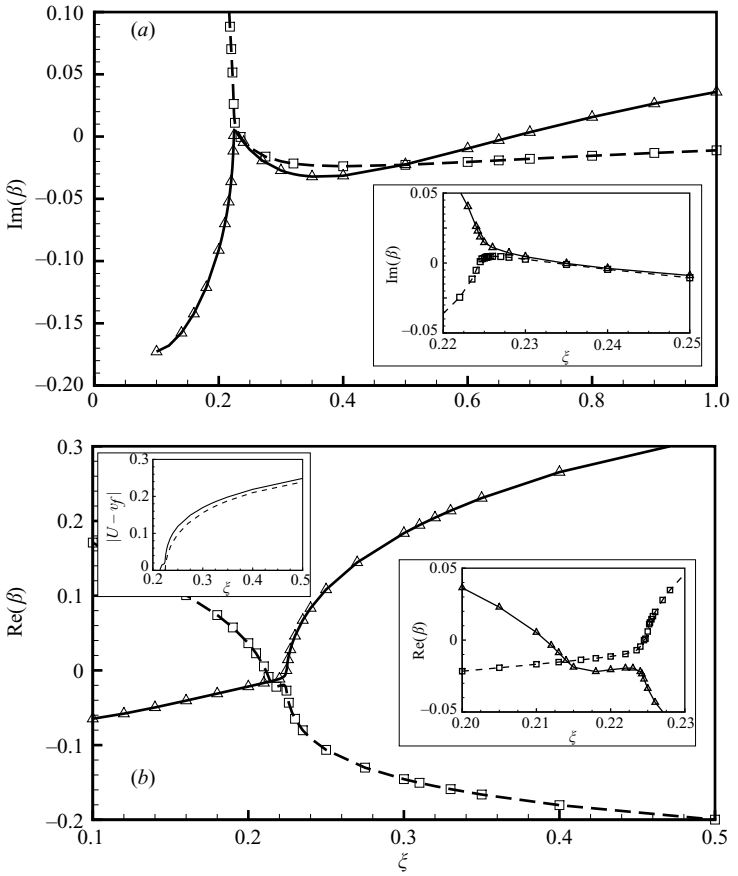


FIGURE 9. As figure 8 but for $Re=10^3$.

takes place similarly to the fixed $Ri$ and variable $\xi$ cases (cf. figures 5, 7 and 10): two K-H modes merge at a certain value of $Ri$ and two conjugate Holmboe modes exit the merging point. Again, these are the Takens–Bogdanov codimension- two bifurcation points, which were observed earlier by Smyth & Peltier (1989).

In the spatial case also (figure 11), the dependence $\beta(Ri)$ is similar to the dependence $\beta(\xi)$ described above (figures 5 and 9), i.e. the transitions between the K-H and Holmboe modes are continuous. The spatial branches of $\mathrm{Im}(\beta)$ have no intersections in the inviscid fluid case (not shown here). In the viscous fluid case these curves intersect (figure 11*a*) and have close amplification rates for $0.1 \leqslant Ri \leqslant 0.2$. Note that maxima of the two Holmboe modes are shifted above and below with respect to the centreline $y=0$ (figure 6). This means that in a fully nonlinear regime both Holmboe modes can grow simultaneously with rather weak interaction between them. The latter is most likely when their amplification rates are close. Note also that the absolute phase velocities grow with the increase of the Richardson number (inset in figure 11*b*). The curves corresponding to the two phase velocities intersect close to $Ri=0.2$. Possibly, these intersections explain the small difference in the phase velocities observed in figures 8(*b*) and 9(*b*).

Similar continuous transformations were observed by Pawlak & Army (1998) for inviscid flow with the density diffusion neglected for tanh velocity and density profiles

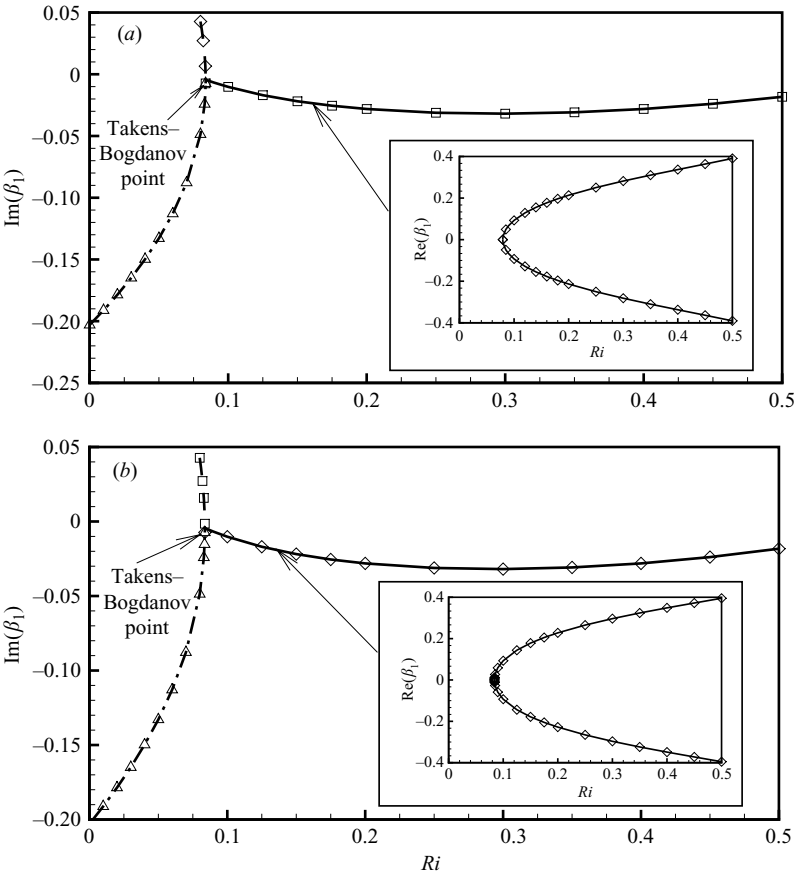


FIGURE 10. Dependence of the time amplification rate $\mathrm{Im}(\beta_1)$ on the Richardson number. Viscous non-isothermal flow. $Pr = 9$, $\lambda = 0.5$, $R = 3$, $\xi = 0.45$, $\alpha_z = 0$. (*a*) Inviscid flow, (*b*) $Re = 10^3$. $\Delta$, first K-H mode; $\square$, second K-H mode; $\diamond$, Holmboe modes. The insets show the dependence of $\mathrm{Re}(\beta_1)$ on $Ri$ for the two Holmboe modes.

and by Ortiz *et al.* (2002) for piecewise linear velocity and stepwise density profiles. It was noticed in both these works that there is no distinct difference between the K-H and Holmboe modes and the transition region was attributed to so-called "hybrid modes". It is shown here that the continuous transformation of the K-H modes into the Holmboe modes takes place also in viscous fluid with the density diffusion accounted for. Furthermore, we show that this transition takes place due to a pair of continuously changing eigenmodes, which means that the spatial K-H or Holmboe modes are, in fact, two possible patterns of the same continuously changing eigenmode (figures 5–11).

The dependence of the parameter $\beta$ on the Reynolds number for various Richardson numbers and fixed layer thickness is shown in figures 12–14. Figure 12 corresponds to the K-H instability. The values of $\mathrm{Im}(\beta_1)$ describing the time amplification rates are shown by open symbols and dashed lines in figure 12(*a*). The spatial amplification rates $\mathrm{Im}(\beta)$ are shown by filled symbols and solid lines. The values of the imaginary part of $\beta$ that correspond to the temporal and spatial instabilities are rather close. The distance between them decreases with the increase of the Richardson number. Since for the K-H instability $\mathrm{Re}(\beta_1) = 0$ these zero values are not shown on the graph.

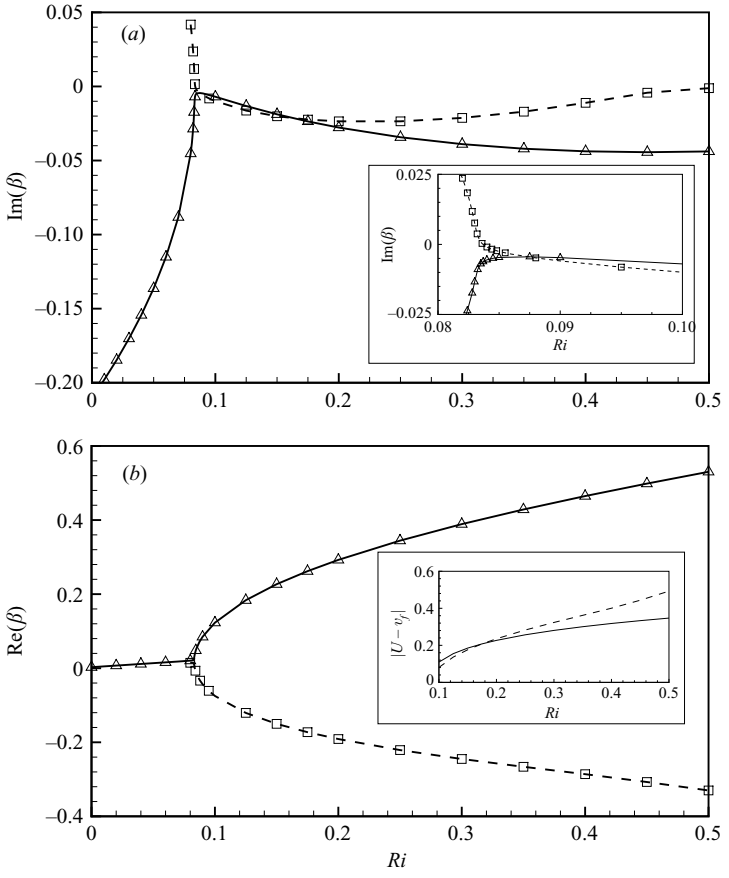


FIGURE 11. Dependence of parameter $\beta$ on the Richardson number for the spatial instability. Viscous non-isothermal flow, $Re = 10^3$, $Pr = 9$, $R = 3$, $\lambda = 0.5$, $\xi = 0.45$, $\alpha_z = 0$. $\Delta$, first K-H–Holmboe mode; $\square$, second K-H–Holmboe mode. The inset in (*a*) zooms in on the transitions from K-H to Holmboe type of instability. An inset in (*b*) shows the absolute difference between the phase velocity of Holmboe modes and average velocity of the base flow.

The real parts of $\beta$ are shown in figure 12(*b*). Here we observe a rather unexpected behaviour: at zero and small Richardson numbers ($Ri \leqslant 0.01$) the values of $\mathrm{Re}(\beta)$ have a sharp maximum at rather small values of the Reynolds number, $Re \approx 50$. With the increase of the Richardson number this maximum is smoothed and for $Ri \geqslant 0.5$ the dependence is monotonic. It is seen (figures 12*a* and 12*b*) that at large Reynolds numbers the values of $\beta$ approach a limiting value, which corresponds to the inviscid fluid case.

Figures 13 and 14 show how the parameter $\beta$ changes with the Reynolds number for the Holmboe instability. Here we must account for the two different Holmboe modes that appear in the spatial case. To differentiate between the two modes, we refer to the one with $\mathrm{Re}(\beta) > 0$ as 'the first' and the other with $\mathrm{Re}(\beta) < 0$ as 'the second' (figures 13*b* and 14*b*). Note that if $\mathrm{Im}(\beta) \ll \mathrm{Re}(\beta)$, which holds for the values shown in figures 13 and 14, a rough estimate of the phase velocity is given by $v_f = \bar{U}/[1+\mathrm{Re}(\beta)]$. Therefore, according to our notation, the first Holmboe mode tends to propagate upstream, while the second tends to propagate downstream, with respect to the mean velocity $\bar{U}$. In the temporal case the two Holmboe modes are conjugate, so that

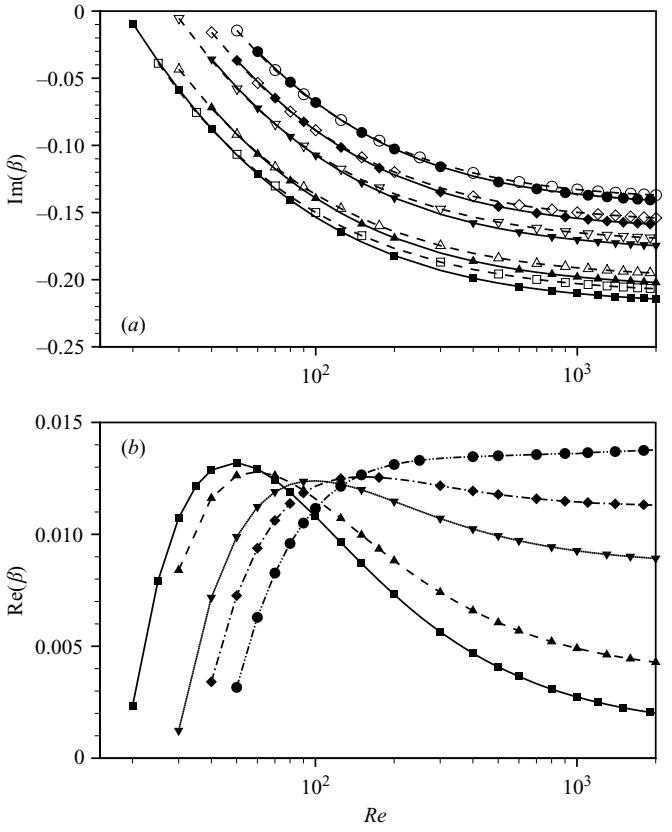


FIGURE 12. Dependence of parameter $\beta$ on the Reynolds number for the temporal (open symbols) and spatial (filled symbols) K-H instability. Viscous non-isothermal flow, $Pr = 9$, $R = 3$, $\lambda = 0.5$, $\xi = 0.45$, $\alpha_z = 0$. □, ■, $Ri = 0$; △, ▲, $Ri = 0.01$; ▽, ▼, $Ri = 0.03$; ◇, ◆, $Ri = 0.04$; ○, ●, $Ri = 0.05$.

for each $\mathrm{Re}(\beta_1)$ of one mode there exits another Holmboe mode with $-\mathrm{Re}(\beta_1)$ and the same imaginary part. Thus, only positive values of $\mathrm{Re}(\beta_1)$ are shown in figure 14(*a*).

The Reynolds-number dependence of the amplification rates of the temporal problem (figure 13*a*) can be described as follows. At relatively small Richardson numbers, $Ri \leqslant 0.3$, the values of $\mathrm{Im}(\beta_1)$ decrease monotonically and at large Reynolds numbers reach a limit value of the inviscid fluid. Note that $\mathrm{Im}(\beta_1) < 0$ indicates instability, so that the perturbations grow faster at larger Reynolds numbers, as expected. However, at large Richardson numbers, $Ri \geqslant 0.5$, the behaviour of the time amplification rates changes qualitatively. The amplification rates reach their minimal values (i.e. maximal amplification) at rather small Reynolds numbers, which are of the order 100, and then increase monotonically, also reaching their limiting values at large *Re*. Thus, at large Richardson numbers the amplification rate of the temporal Holmboe modes increases rapidly with the increase of the Reynolds number from zero to approximately 100, and then decreases with the further growth of *Re*. Note also that in the region of non-monotonic dependence the amplification rate sometimes increases with increase of the Richardson number (cf. curves of $Ri = 0.4$ and 0.5 in figure 13*a*). The growth of amplification rates with the decrease of the Reynolds number (increase of viscosity) and increase of the Richardson number (increase

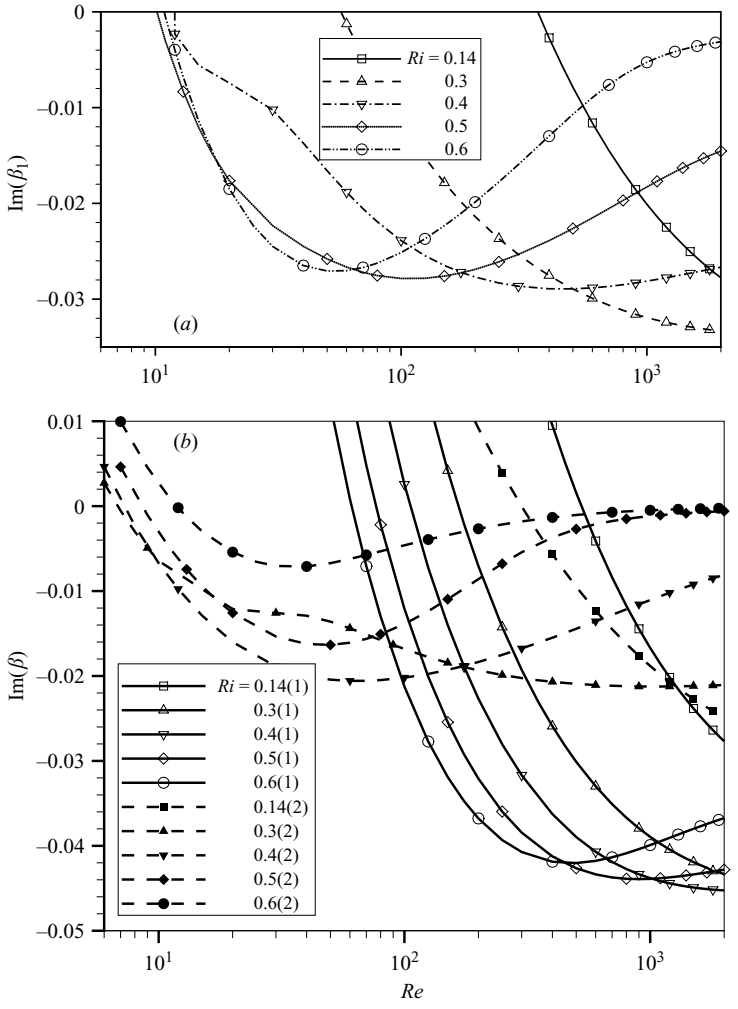


FIGURE 13. Dependence of Im($\beta$) on the Reynolds number for the temporal ($a$) and spatial ($b$) Holmboe instability. Numbers in brackets in ($b$) indicate the first and the second spatial Holmboe modes. The results are shown for Im($\beta$) $\leqslant 0.01$. Viscous non-isothermal flow, $Pr = 9$, $R = 3$, $\lambda = 0.5$, $\xi = 0.45$, $\alpha_z = 0$. □, ■, $Ri = 0.14$ △, ▲, $Ri = 0.3$; ▽, ▼, $Ri = 0.4$; ◇, ◆, $Ri = 0.5$; ○, ●, $Ri = 0.6$.

of stable stratification) is quite abnormal and indicates the possibility of a three-dimensional primary instability (Smyth & Peltier 1990). This issue is studied in § 3.5.

The spatial amplification rates of the two Holmboe modes exhibit qualitatively different dependence on the Reynolds number (figure 13$b$). The magnitudes of Im($\beta$) of the first mode, shown by the open symbols, increase monotonically with an increase of the Reynolds number for $Ri \leqslant 0.4$. At larger Richardson numbers the magnitude of Im($\beta$) has a weak maximum at a Reynolds number of several hundred. The values of Im($\beta$) of the second mode also decrease monotonically for $Ri \leqslant 0.3$, but at larger Richardson numbers have a sharp minimum at $Re < 70$. Comparison of figures 13($a$) and 13($b$) shows that the $Re$-dependence of the amplification rates of the second Holmboe modes, which tend to propagate downstream, is similar to that of the temporal modes. At the same time the $Re$-dependence of the amplification rates of

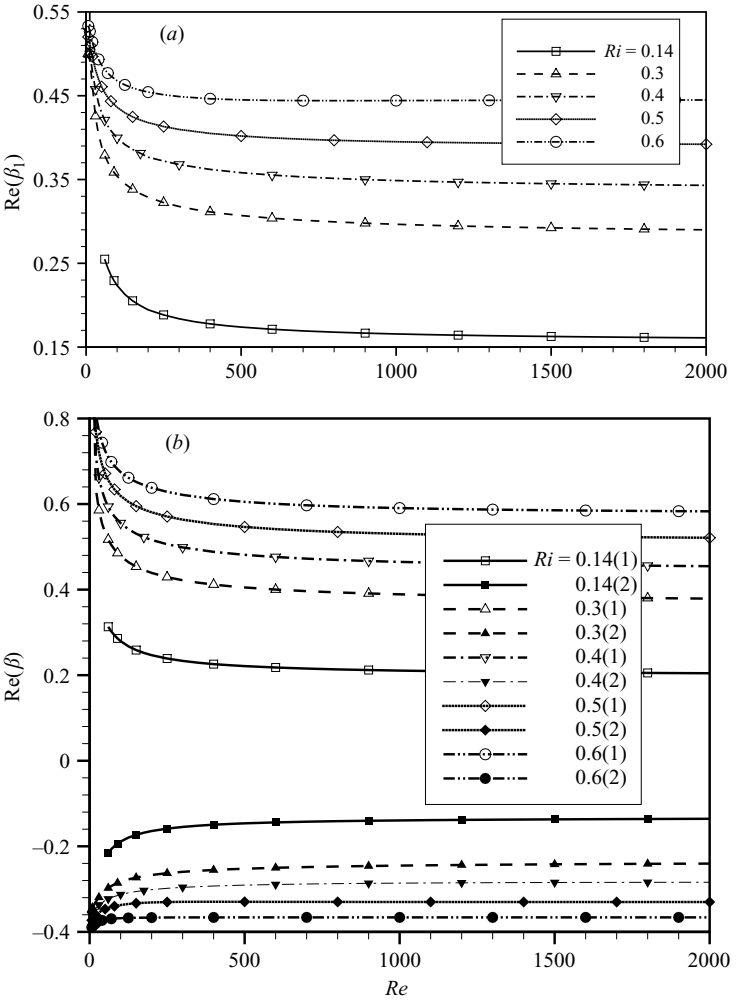


FIGURE 14. For caption see next page.

the first Holmboe modes, which tend to propagate upstream, is different. At small Reynolds number the first Holmboe mode is stable (figure 13*b*); however at large Reynolds number its amplification rate becomes significantly larger than that of the second mode. For each *Ri* there are intersection points at which amplification rates of both Holmboe modes are equal, which can lead to an interesting nonlinear interaction between them. In general, the nonlinear development of the Holmboe instability at small and large Reynolds numbers is expected to be qualitatively different.

Figure 14 shows how Re($\beta$) varies with the increase of the Reynolds number. Here all the dependence are monotonic. The absolute values of Re($\beta$) grow with the increase of the Richardson number (as was observed in figures 10 and 11) and decrease with the increase of the Reynolds number. Figure 14(*c*) compares the absolute phase velocities of the two Holmboe modes, from which we again see that the difference between the phase velocities increases with the increase of the Richardson number. Zhu & Lawrence (2001) observed the upstream and downstream Holmboe waves moving with different phase velocities in an experiment where the Reynolds number

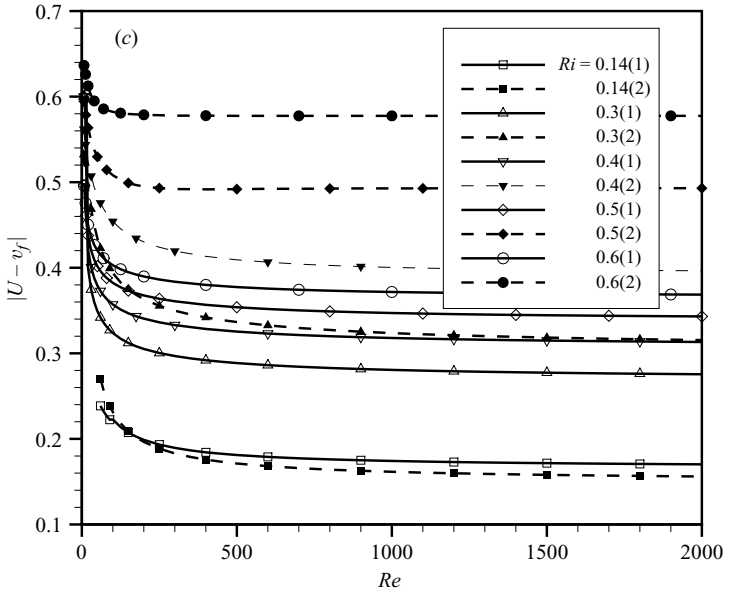


FIGURE 14. Dependence of Re($\beta$) on the Reynolds number for the temporal ($a$) and spatial ($b$) Holmboe instability. Numbers in brackets ($b$) indicate the first and the second spatial Holmboe modes. Viscous non-isothermal flow, $Pr=9$, $R=3$, $\lambda=0.5$, $\xi=0.45$, $\alpha_z=0$. □, ■, $Ri=0.14$ △, ▲, $Ri=0.3$; ▽, ▼, $Ri=0.4$; ◇, ◆, $Ri=0.5$; ○, ●, $Ri=0.6$, ($c$) Absolute difference between the phase velocity of Holmboe modes and average velocity of the base flow. Parameters as ($a$, $b$).

was below 5000 and ascribed the difference to the shift between the density and velocity interfaces. Here we show that different phase velocities should be expected in viscous flow even if the shift is completely removed.

### 3.5. *Gaster transformation*

In this Section we discuss in which cases the temporal and spatial problems considered here are connected with the Gaster transformation. To do this we express the group velocity of a spatial disturbance as a function of the governing parameters. Assuming the dimensionless wavenumber $\alpha=\alpha_r+\mathrm{i}\alpha_i$ of the spatial disturbance is a function of $\xi$, $\lambda$, $Re$ and $Ri$, we obtain the dimensional wavenumber $\tilde{\alpha}$ as

$$\tilde{\alpha}=\alpha[\xi(\omega_0),\, Re(\omega_0),\, Ri(\omega_0),\, \lambda]\frac{2\omega_0}{U_1+U_2} \tag{25}$$

where we emphasize that $\xi$, $Re$ and $Ri$ are also functions of $\omega_0$, e.g. $\xi=\delta(U_1+U_2)/2\omega_0$. The expressions for $Re$ and $Ri$ are given in Table 1. Calculating the dimensional group velocity as $1/\tilde{c}_g=\partial\tilde{\alpha}_r/\partial\omega_0$ and rendering it dimensionless we obtain (recall $\alpha=1+\beta$, and denote $\beta=\beta_r+\mathrm{i}\beta_i$)

$$\frac{1}{c_g}=\frac{U_2-U_1}{\tilde{c}_g}=-2\lambda\left(1+\beta_r+\xi\frac{\partial\beta_r}{\partial\xi}-Ri\frac{\partial\beta_r}{\partial Ri}-Re\frac{\partial\beta_r}{\partial Re}\right). \tag{26}$$

One equality $\omega_{r,spatial}=\omega_{r,temporal}$ is exactly satisfied for the K-H instability in the reference frame moving with the average velocity $\bar{U}=(U_1+U_2)/2$ The other equality of the Gaster transformation $\tilde{\alpha}_{temporal}=\tilde{\alpha}_{spatial}$ is approximately satisfied for the considered problem if $|\beta_r|\ll 1$. However, in the case of Holmboe instability

| $\lambda$ | $Ri$ | $Re$ | $\beta_1^i$ | $\beta_r$ | $\beta_i$ | $\partial\beta_r/\partial\xi$ | $\partial\beta_r/\partial Ri$ | $\partial\beta_r/\partial Re$ | $\beta_1^i/\beta_i$ | r.h.s. of (27) |
|---|---|---|---|---|---|---|---|---|---|---|
| 0.5 | 0 | inviscid | −0.349 | −0.0812 | −0.344 | 0.0498 | – | – | 1.0145 | 1.0384 |
| 1 | 0 | inviscid | −0.69725 | −0.3594 | −0.60165 | 1.125 | – | – | 1.1589 | 1.0776 |
| 0.5 | 0 | 1000 | −0.32800 | −0.07220 | −0.32443 | 0.4296 | – | −0.000058 | 1.0110 | 0.9665 |
| 0.5 | 0 | 100 | −0.23227 | −0.02960 | −0.23503 | 0.2014 | – | −0.000291 | 0.9883 | 0.9809 |
| 1 | 0 | 100 | −0.46455 | −0.14549 | −0.47961 | 0.7386 | – | −0.01360 | 0.9686 | 0.71166 |
| 0.5 | 0.1 | inviscid | −0.26946 | −0.05539 | −0.26733 | 0.51686 | 0.2654 | – | 1.0080 | 0.9895 |
| 0.5 | 0.1 | 1000 | −0.24278 | −0.04746 | −0.24133 | 0.4390 | 0.2502 | $0.68\times10^{-5}$ | 1.0060 | 0.9958 |
| 0.5 | 0.1 | 100 | −0.12132 | −0.01174 | −0.12233 | 0.1678 | 0.1630 | −0.000204 | 0.9917 | 0.9874 |

TABLE 2. Several examples for the check of applicability of Gaster transformation. $\xi = 0.2$.

the temporal case is characterized by the two values $\pm\omega_{r,temporal} \neq 0$ having equal magnitudes and opposite signs. The computed $\beta_r$ are also of order 1 and far from being small, so that in the framework of the current study we do not satisfy either of these two equalities of the Gaster transformation. Therefore, in the case of the Holmboe instability the Gaster transformation cannot be applied to the temporal and spatial problems considered here.

The relation between amplifications rates of the Gaster transformation $\omega_{i,temporal}/\alpha_{i,spatial} = -c_g$ also should be evaluated in the moving reference frame. Recalculating $\tilde{c}_g$ in the moving reference frame and using (26) we conclude that this equality is satisfied approximately if

$$\frac{\beta_1^i}{\beta_i} \approx \frac{1}{2}\left(1 + \frac{1}{1 + \beta_r + \xi\dfrac{\partial\beta_r}{\partial\xi} - Ri\dfrac{\partial\beta_r}{\partial Ri} - Re\dfrac{\partial\beta_r}{\partial Re}}\right). \tag{27}$$

We can expect that the Gaster transformation will be valid for the K-H instability in inviscid non-stratified fluid at small $\xi$. In this case the two last terms of the denominator of (27) should be dropped. According to figure 2(*b*) the derivative $\partial\beta_r/\partial\xi$ is small for $\lambda \leqslant 0.5$, and the values of $\beta_i$ and $\beta_1^i$ are close. This agrees with the conclusion of Monkewitz & Huerre (1982) for small $\lambda$. However, at $\lambda = 1$ the derivative $\partial\beta_r/\partial\xi$ becomes large, so that validity of the Gaster transformation must be checked. It must be checked also for the K-H instability in viscous and stratified fluid.

Several examples of valid and invalid Gaster transformation are shown in table 2 for $\xi = 0.2$ and K-H instability. The derivatives needed for evaluation of (27) were calculated by finite differencing. In the case of the K-H instability $\beta_1^r = 0$, so it is necessary that $|\beta_r| \ll 1$ and that approximate equality (27) holds. The latter can be checked by comparison of the two last columns of table 2. We observe that at $\lambda = 0.5$ the Gaster transformation is valid for all cases of the K-H instability including relatively large viscosity at $Re = 100$ and relatively large stratification at $Ri = 0.1$. However, it becomes invalid at $\lambda = 1$, for which values of $\beta_r$ and $\partial\beta_r/\partial\xi$ are not small. An additional check was made for $\xi = 0.6$ and it was found that for $\lambda = 0.5$ the Gaster transformation remains valid for $Re \geqslant 100$ and $Ri \leqslant 0.1$, while is not valid when $\lambda$ reaches unity. Ortiz *et al.* (2002) explained the loss of validity of the Gaster transformation at $\lambda = 1$ by the fact that at this velocity ratio the instability of an inviscid piecewise linear mixing layer flow changes from convective to absolute. Our results show that this conclusion is retained for a continuous velocity profile, as well as for viscous mixing layer flows.

### 3.6. *Neutral stability curves*

In a viscous flow case there exists a critical Reynolds number below which, at given other parameters, the mixing layer is stable. It should be noted that in the viscous and thermally conducting fluid the tanh-profiles (22) are not solutions of the governing equations. Therefore, we assume that the amplification rates are much larger than the rates of viscous dissipation and heat conduction even when the governing parameters are close to their marginal stability values. On the other hand, we can formalize the stability problem in the following way. Consider the flow governed by a volumetric force and a heat source, which yield the solution of steady governing equations in the form of (4), (10) and (22). Then the stability of this solution will be described by (13) and (14) and the whole solution procedure applies without a change. In this Section we report how the critical Reynolds number varies with the thickness of the mixing layer $\xi$ for several values of the Richardson number and fixed values of the Prandtl number and the parameter $R$. The critical Reynolds number corresponds to $\mathrm{Im}(\omega)=\mathrm{Im}(\beta_1)=0$ for the temporal and $\mathrm{Im}(\alpha)=\mathrm{Im}(\beta)=0$ for the spatial cases, respectively.

We consider first the K-H instability. In the temporal case this instability is monotonic, so that $\mathrm{Re}(\omega)=\mathrm{Re}(\beta_1)=0$. Therefore, at the instability threshold $\omega$ and $\beta_1$ are complex zeros. In the spatial case the value of $\mathrm{Re}(\beta)$ is not necessarily zero. However, it is easy to see that if $\beta_1=0$ is an eigenvalue of (20) and (21) for $\beta_0=0$ and other parameters given, then $\beta_k=0$ will also be an eigenvalue with the same eigenvector for any $k$ including $k\to\infty$. This means that the eigenvector of the temporal problem (16) corresponding to the eigenvalue $\omega=0$ is also the eigenvector of the spatial problem corresponding to $\beta=0$, so that the critical values of parameters of the temporal and spatial problems coincide for K-H instability. The spatial instability starting from $\beta=0$ ($\alpha=1$) means a continuous branching from stable to unstable flow. It is possible that in the spatial problem there are other instabilities for which $\mathrm{Re}(\beta)\neq 0$. If such instability is of the K-H type it would mean that the branching is not continuous and the value of $\beta$ undergoes a jump. In the calculations reported, however, all such thresholds were observed only for sufficiently large Richardson numbers and were attributed to the Holmboe instability, rather than to the K-H instability.

The neutral stability curves calculated for small Richardson numbers and corresponding to the K-H instability are shown in figure 15. As explained above, these curves describe the onset of both the temporal and spatial instabilities. The flows are unstable below the curves at large enough Reynolds numbers and small enough layer thicknesses. At large Reynolds numbers all the curves reach the asymptotic $\xi$-values that correspond to the $\xi$-stability limit of the inviscid fluid.

Figure 16 shows the temporal neutral stability curves for moderate Richardson numbers, $0.1\leqslant Ri\leqslant 0.3$. To illustrate the transition between the K-H and Holmboe modes along the neutral curves the case of $Ri=0.1$ is shown separately in figure 16($a$). At small Reynolds number and small values of $\xi$ the instability sets in due to the K-H monotonic mode. The Holmboe modes become unstable at larger values of $\xi$ and larger Reynolds number. Thus, for $Ri=0.1$ the Holmboe mode becomes dominant for $\xi\geqslant 0.405$ (figure 16$a$). For $Re>750$ the instability sets in due to the K-H mode at small $\xi$ and due to the Holmboe mode at large $\xi$. Note that for $560<Re<750$ there is a region between the K-H and the Holmboe neutral curves in which the flow remains stable, while it is unstable above and below this region. As shown in the previous Section, the transition between the K-H and Holmboe modes takes place via the Takens–Bogdanov bifurcation. The dashed line in figure 16($a$) shows the calculated

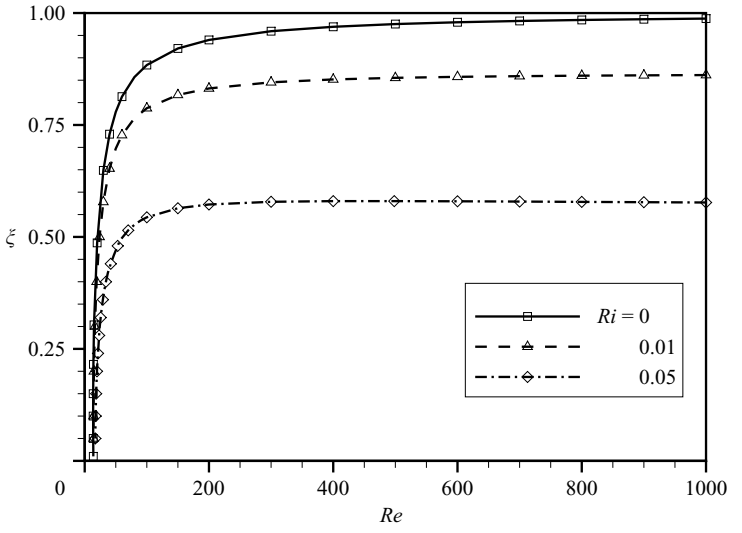


FIGURE 15. Neutral stability curves for the K-H temporal and spatial instability. The mixing layer flow is unstable below the curves and is stable above them. $Pr = 9$, $R = 3$, $\lambda = 0.5$, $\alpha_z = 0$.

Takens–Bogdanov points, which lie very close to the straight line $\xi = 0.405$. Clearly, similar lines exist at other Richardson numbers, so that there is a surface in the $Ri$–$R$–$\xi$ space at which the Takens–Bogdanov bifurcation takes place. The location of such lines can be easily derived from analytical dispersion relations when they are known (e.g. Holmboe 1962; Caulfield 1994; Ortiz *et al.* 2002). Here we show that the transition remains similar also for continuous density and velocity profiles and with the effects of viscosity and density diffusion accounted for.

When the Richardson number increases above the value of 0.1 the neutral curves exhibit a similar behaviour (figure 16*b*). The distance between the K-H and Holmboe curves grows with the growth of $Ri$. The points where the two modes merge are beyond $Re = 1000$ and are not shown on the graph. Further increase of the Richardson number suppresses the instability due to the K-H mode. However, as was argued above, the Holmboe mode still can be found. This is illustrated in figure 17. Unfortunately, we were unable to continue the calculations beyond $Ri = 0.5$ because of a fast slowing down of the convergence. In general, we observe that the amplification rates decay with the increase of $Ri$; however the flow never becomes definitely stable at any $\xi$ and $Re$.

To complete the description of the neutral stability curves it is necessary to show how the frequency (or the value of $\mathrm{Re}(\beta_1)$) of the neutral Holmboe modes changes with the Reynolds number. This is done in figure 18. It is interesting that at sufficiently large $Re$ the frequency remains almost constant along the upper branch of the neutral curve, while it decreases with the increase of $Re$ along the lower branch.

The neutral stability curves corresponding to the spatial instability are shown in figure 19. As explained above, the spatial and temporal K-H instabilities set in at the same Reynolds numbers, so that the neutral curves shown in figure 15 for the small Richardson numbers correspond to both spatial and temporal cases. The neutral curves shown in figure 16 are repeated in figure 19 as dashed lines. Since the spatial Holmboe instability is described by the two different modes we calculated the neutral curve for each Holmboe mode separately. The corresponding neutral curves are shown in figure 19 by the dash-and-dot and solid lines for the first and the second mode,

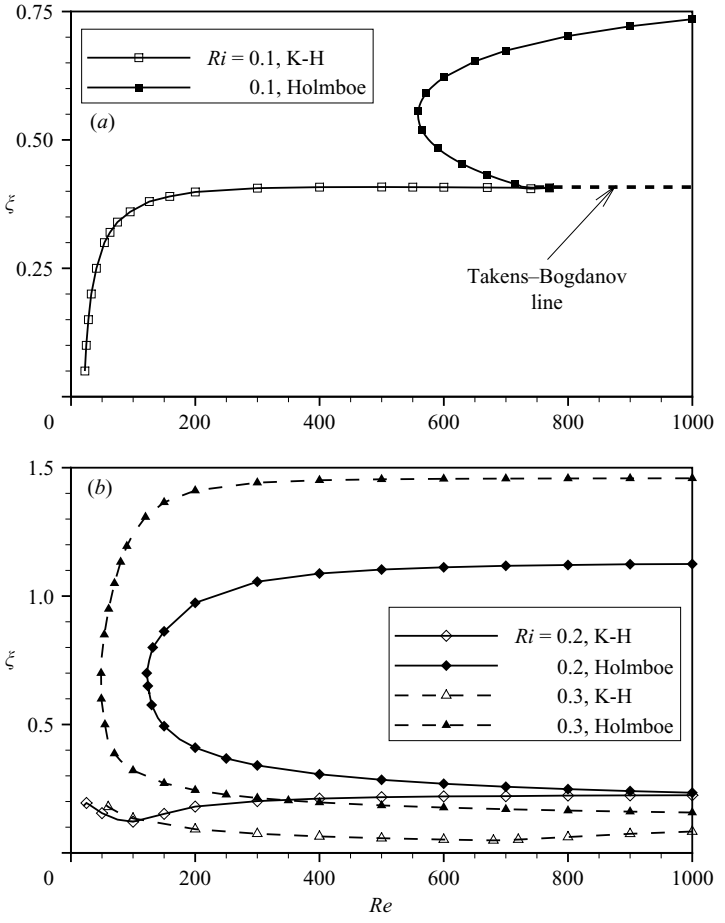


FIGURE 16. Neutral stability curves for the K-H (empty symbols) and Holmboe (filled symbols) temporal instability at moderate Richardson numbers. (*a*) $Ri = 0.1$, (*b*) $Ri = 0.2$ and 0.3. The mixing layer flow is unstable below the K-H curves and inside the Holmboe curves. $Pr = 9$, $R = 3$, $\lambda = 0.5$, $\alpha_z = 0$.

respectively. It was observed that the second Holmboe mode, which corresponds to $\mathrm{Re}(\beta) < 0$, had already become dominant at small Reynolds numbers (figure 13*b*). This is replicated in the neutral curves: the second Holmboe mode become unstable before the first one. Thus, with the gradual increase of the Reynolds number the Holmboe wave propagating downstream with the mean flow will be observed first. However, at large Reynolds number the mode propagating upstream can attain a larger amplification rate (figure 13*b*). The problem of nonlinear interaction of these two modes is beyond the scope of present study.

As in the temporal case, the neutral curves of the spatial Holmboe modes (figure 19) must be followed by the corresponding dependence of $\mathrm{Re}(\beta)$, shown in figure 20. End points and turning points of some curves in figures 19 and 20 are indicated by letters to show how the curves in the two figures relate to each other. Note that at the upper parts of the Holmboe neutral curves the spatial period of the perturbation $\alpha = 1 + \mathrm{Re}(\beta)$ is almost independent of the Reynolds number, while at their lower parts this dependence is significant. It is also observed that with the growth of the Richardson number the correction $\mathrm{Re}(\beta)$ to the excitation period $\alpha = 1$ grows and

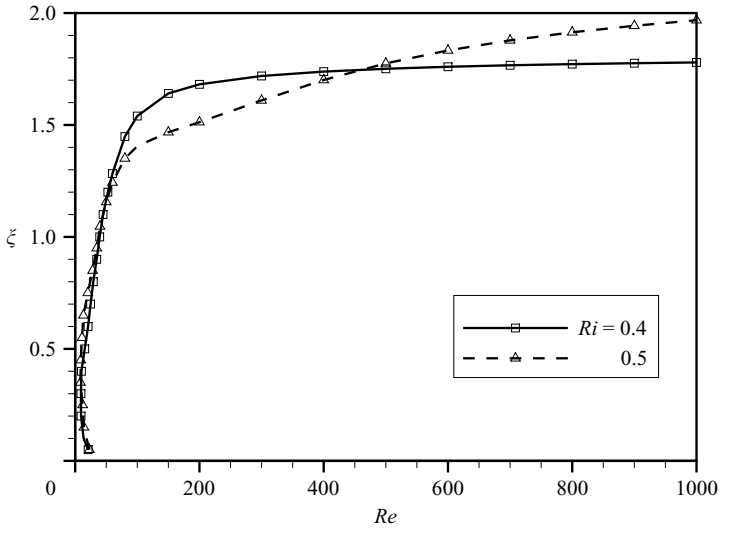


FIGURE 17. Neutral stability curves for the Holmboe temporal instability at large Richardson numbers. The mixing layer flow is unstable below the curves and is stable above them. $Pr = 9$, $R = 3$, $\lambda = 0.5$, $\alpha_z = 0$.

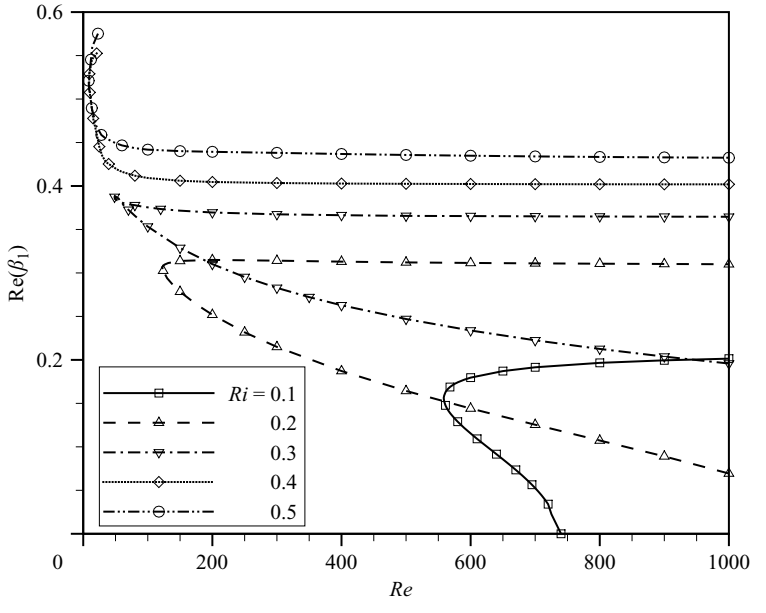


FIGURE 18. Values of $\mathrm{Re}(\beta_1)$ of the Holmboe modes corresponding to the neutral stability curves shown in figures 16 and 17. Upper and lower parts of the curves in this figure relate to the upper and lower parts of the corresponding neutral curves. $Pr = 9$, $R = 3$, $\lambda = 0.5$, $\alpha_z = 0$.

at $Ri = 0.3$ has already reached 45 % for the first and 30 % for the second Holmboe modes.

### 3.7. *Three-dimensional primary instability*

Smyth & Peltier (1990) showed that at large Richardson and small Reynolds numbers the primary temporal Holmboe instability can be three-dimensional. This can happen

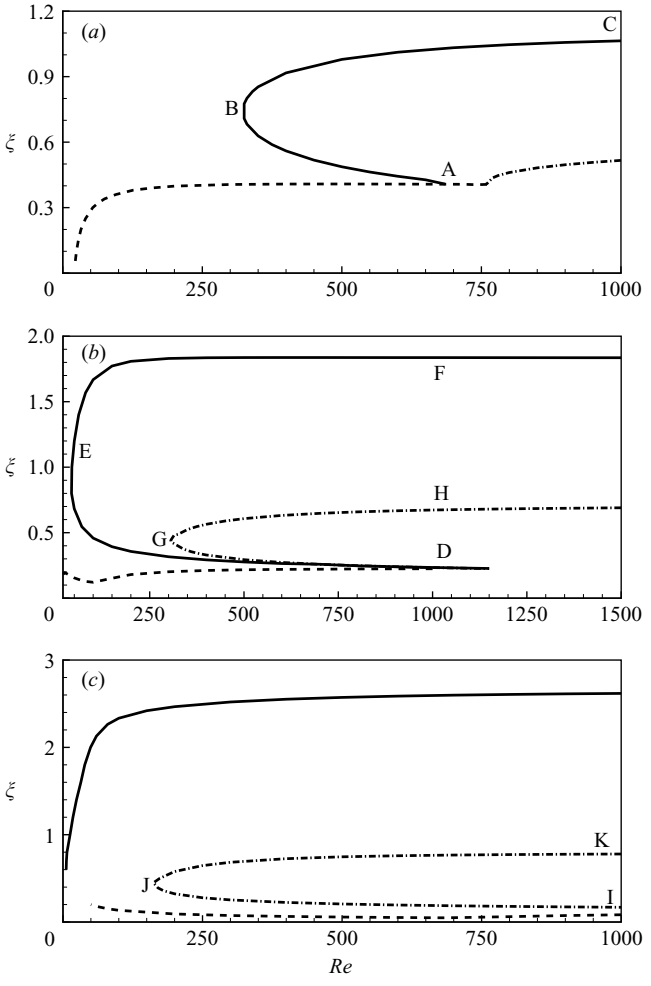


FIGURE 19. Neutral stability curves for the spatial instability. The mixing layer flow is unstable below or inside the curves the curves. $Pr = 9$, $R = 3$, $\lambda = 0.5$. Dashed lines, K-H modes; dash-and-dot lines, first Holmboe mode; solid lines, second Holmboe mode. (*a*) $Ri = 0.1$, (*b*) $Ri = 0.2$, (*c*) $Ri = 0.3$, $\alpha_z = 0$.

if the amplification rate grows either with the increase of the Richardson or decrease of the Reynolds number. Examination of the dependence $\beta_1(Re, Ri)$ reported above shows that both tendencies are observed in figure 13(*a*) for $0.3 \leqslant Ri \leqslant 0.5$ and $30 \leqslant Re \leqslant 100$. A similar behaviour is also characteristic for the second spatial Holmboe mode in approximately the same range of parameters (figure 13*b*). However the arguments of Smyth & Peltier (1990) made for the temporal amplification rate cannot be extended to the spatial case. Therefore, it would be interesting to check whether a primary three-dimensional instability can be observed for the spatially growing perturbations.

To check this issue we carried out computations of the temporal and spatial growth rates for gradually increasing $\alpha_z$, $\xi = 0.45$, and several fixed values of $Ri$ and $Re$. The results of these computations are shown in figures 21 and 22. It is seen that there exists a rather narrow region where the most unstable perturbation is three-dimensional. The minimal values of $\mathrm{Im}(\beta_1)$ and $\mathrm{Im}(\beta)$, which correspond to the largest

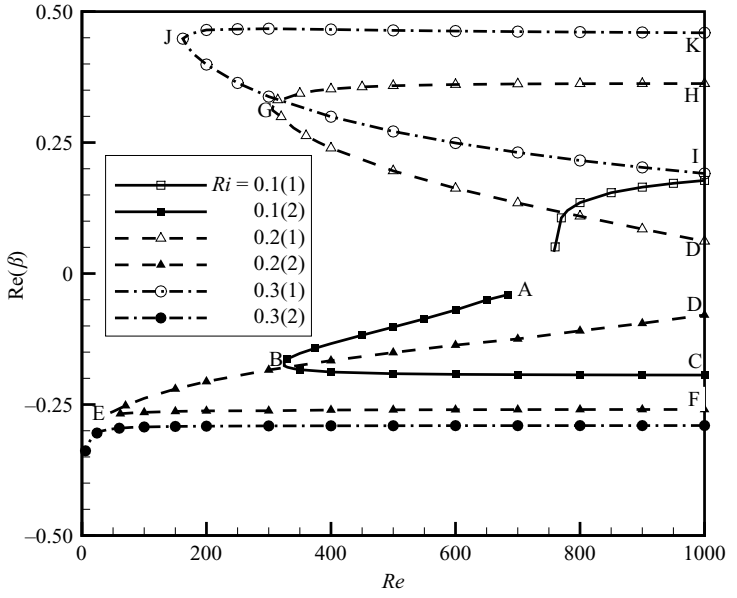


FIGURE 20. Values of Re($\beta$) of the Holmboe modes corresponding to the neutral stability curves shown in figure 19. $Pr = 9$, $R = 3$, $\lambda = 0.5$, $\alpha_z = 0$.

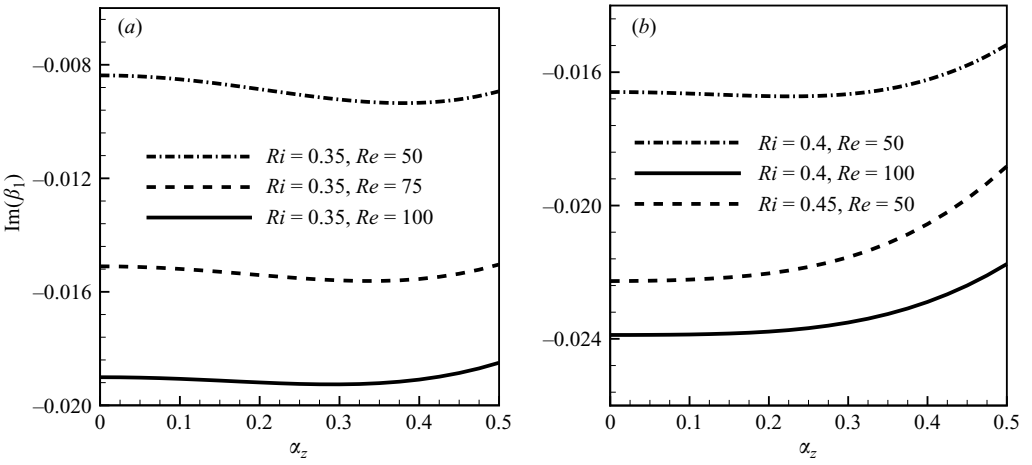


FIGURE 21. Dependence of temporal amplification rates on spanwise wavenumber. Holmboe modes. $Pr = 9$, $R = 3$, $\lambda = 0.5$, $\xi = 0.45$.

three-dimensional amplification rates, smooth out rather quickly with the growth of the Reynolds number. Furthermore, an increase or decrease of the Richardson number leads to a disappearance of the minima (figures 21*b* and 22*b*). Note that the spatial instability corresponds to the second Holmboe mode with Re($\beta$) < 0 which propagates upstream with respect to the mean velocity of the base flow.

An additional question is how the existence of the area of three-dimensional primary instability will alter the neutral stability curves shown in figures 16, 17 and 19. To provide a complete answer to this question it is necessary to localize the maxima of the three-dimensional amplification rates for various values of $\xi$, which would require

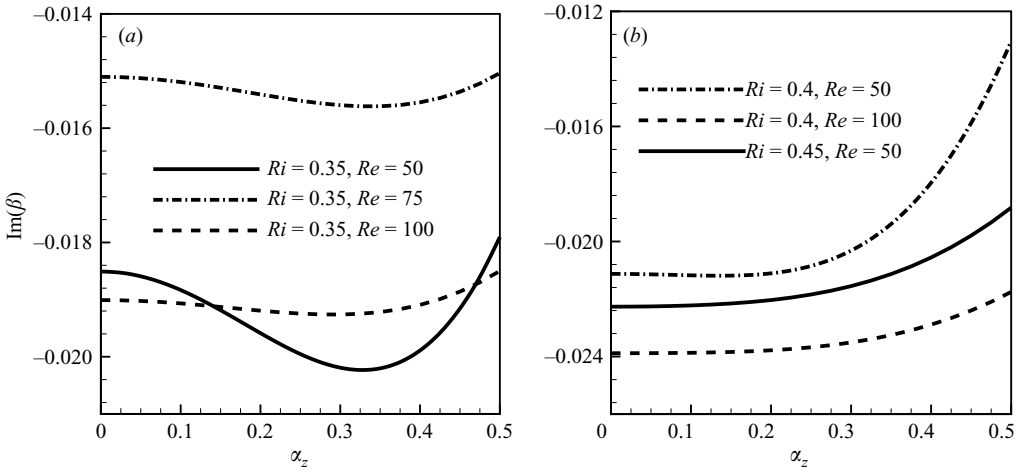


FIGURE 22. Dependence of spatial amplification rates on spanwise wavenumber. Second Holmboe mode. $Pr = 9$, $R = 3$, $\lambda = 0.5$, $\xi = 0.45$.

an extremely large amount of computation. It was found that in the case of spatial instability the area of most unstable three-dimensional perturbations lies inside the unstable area bounded in figure 19 by the neutral curve. In the case of the temporal instability the neutral curves corresponding to $0.3 \leqslant Ri \leqslant 0.4$ will be slightly altered in the area of small Reynolds numbers, so that the area corresponding to unstable states will be enlarged.

## 4. Conclusions

A simple iterative procedure yielding the solutions of the temporal and spatial stability problems for a parametrically excited stratified mixing layer has been developed. Using this procedure, a parametric study of the temporal and spatial instabilities in the stratified mixing layer with hyperbolic tangent velocity and temperature profiles was carried out. The procedure can be used for other mixing layer profiles (e.g. piecewise-linear profiles) and can be easily extended to other plane-parallel shear flows with parametric excitation of instability.

We have found that in the case of inviscid isothermal fluid flow the temporal and spatial perturbation profiles are close for modest values of the velocity ratio $\lambda \leqslant 0.5$. The properly rescaled temporal and spatial growth rates are also close. When the value of $\lambda$ approaches unity the perturbations and growth rates differ, especially for thin mixing layers with $\xi \leqslant 0.2$ (figures 1 and 2). Compared to the inviscid case, the viscous flow problem is characterized by smaller temporal and spatial amplification rates and narrower intervals of $\xi$ in which the instability is observed. At the same time, the difference between temporal and spatial perturbation patterns decreases with the increase of viscosity (figures 2 and 3).

It was shown that the transition between the temporal K-H and Holmboe instability modes takes place via a Takens–Bogdanov codimension- two bifurcation (Kuznetsov 2004). Contrary to the temporal case, the spatial K-H and Holmboe modes continuously transform into one another. Such Takens–Bogdanov points and continuous transforms were observed in the planes $Re$–$\xi$ (figures 4, 7, 10, 16) and $Re$–$Ri$ (figures 5, 8, 9, 11). We concluded that that there exists a surface in the $Re$–$Ri$–$\xi$

space at which the Takens–Bogdanov bifurcation takes place. Taking into account the results of Smyth & Peltier (1989), obtained for other values of $Pr$ and $R$, we conclude that these transitions are common for stratified mixing layers and can be expected also for background velocity and temperature profiles different from those considered here. For example, the lines separating the temporal K-H and Holmboe instabilities can be easily derived from analytical dispersion relations when such relations are known (e.g. Holmboe 1962; Ortiz *et al.* 2002).

In spite of the qualitative difference in the transitions between K-H and Holmboe instabilities in the temporal and spatial formulations, the spatial and temporal perturbations corresponding to the Holmboe modes retain similar profiles (figure 8). It is also emphasized that the Holmboe perturbation profiles are similar to those of the K-H ones. This similarity together with the observed continuous transitions between the two instabilities led to an important conclusion: the origin of the K-H and Holmboe instabilities should be explained in the framework of a common physical mechanism related to competition between shear and stratification. The interaction between instabilities induced by shear in the upper and lower layers usually is responsible for the K-H mode. At smaller stratification, the interaction of shear and stratification induces the second K-H mode. With the increase of stratification the interaction between shear and buoyancy leads to a continuous transition of these two spatial K-H modes into two spatial Holmboe modes. In the temporal configuration the interaction between a growing perturbation and the mean flow leads to either monotonic growth (K-H instability) or oscillatory growth (Holmboe travelling waves). In the spatial configuration the terms 'monotonic' and 'oscillatory' cannot be applied since oscillations along the streamwise axis are always present and develop due to the spatial wavenumber. In the spatial case the K-H and Holmboe modes can be distinguished either by the location of the maximum of the perturbation of streamwise velocity or by the difference between the actual spatial wavelength and the wavelength of the exciting perturbation: small differences correspond to K-H and the large differences to Holmboe instability. Instead of the difference of wavelengths one may employ the difference between the mean velocity of the base flow and the phase velocity of the unstable mode. The definition is similar, i.e. a small difference corresponds to K-H and a large difference to the Holmboe instability. Since the transition between the two instabilities is continuous there is no clear criterion that allows one to distinguish between them.

It is shown also that with the increase of viscosity the transition between the K-H and Holmboe instabilities can shift into the region of decaying perturbations (figure 11). This implies that with the growth of the Richardson number or layer thickness a laboratory or numerical model will show a disappearance of the K-H instability before the Holmboe instability sets in. This may give an impression that the modes are separated, which is wrong according to the present results.

It is found that with the growth of the Reynolds number the K-H and Holmboe modes exhibit different behaviour (figures 12–14). The amplification rates of the temporal and spatial K-H modes remain close. The correction of the spatial period, $\mathrm{Re}(\beta)$, of these modes remains small and at small Richardson numbers has a maximal value at rather small Reynolds number (e.g. near $Re \approx 50$ for $\xi = 0.45$). This implies, in particular, that the phase velocity of the spatial K-H modes remains close to the average velocity of the mean flow, at least for parameters close to the marginal stability limit. The time amplification rates of the temporal Holmboe modes grow with the increase of the Reynolds number when the bulk Richardson number is below 0.3. At larger Richardson number the dependence becomes non-monotonic, so that the

amplification rates are maximal at a certain Reynolds number and then unexpectedly decrease with the growth of *Re* (figure 13*a*). The amplification rates of the two spatial Holmboe modes exhibit different Reynolds number dependencies (figure 13*b*). An important observation is that at small Reynolds number the amplification rate of the Holmboe wave propagating downstream is larger, while at large Reynolds number the upstream propagating waves begin to grow faster. It should be emphasized also that the spatial periods of the two spatial Holmboe modes, as well as their absolute phase velocities, are different and that their most intensive parts are located on different sides of the mixing layer centreline. Based on these observations we expect a rather complicated interaction of these modes in a fully nonlinear regime.

On the basis of the model of the parametrically forced mixing layer considered we derived an expression for calculation of the group velocity. This allowed us to check whether the two associated temporal and spatial problems considered here are connected through the Gaster transformation. It is shown that the Gaster transformation is valid for the K-H instability at small values of the velocity ratio $\lambda \leqslant 0.5$. When $\lambda$ approaches unity the Gaster transformation becomes invalid.

We argued that the critical parameters, e.g. the critical Reynolds number, corresponding to the onset of instability due to the K-H modes are the same for both spatial and temporal formulations. However, they are different for the temporal and spatial Holmboe modes. It should be noted that with the increase of the Reynolds number from a small value to the critical value the spatial Holmboe instability sets in as a wave propagating downstream. Another wave, propagating upstream, becomes unstable at larger Reynolds number and its amplification rate becomes comparable to that of the downstream wave only with a significant increase of the Reynolds number.

We have shown also that, along with the primary three-dimensional temporal instability discovered by Smyth & Peltier (1989), there exists a primary spatial three-dimensional instability. This instability can be observed at large Richardson and low Reynolds numbers. In the spatial case it sets in as an oblique wave propagating upstream along the streamwise coordinate.

The computations reported show that the difference between the temporal and spatial instabilities of the stratified mixing layer flow is most pronounced at large Richardson numbers when the Holmboe instability becomes dominant. The results of linear stability analysis allow us, in particular, to pose the most interesting problems for further nonlinear studies. These, in our opinion, are a study of nonlinear transitions between spatial K-H and Holmboe modes, and a study of the interaction of two spatial Holmboe modes at large Richardson and Reynolds numbers.

This work is supported by the Israel Science Foundation (Grant 240/01).

## REFERENCES

Baines, P. G. & Mitsudera, H. 1994 On the mechanism of shear flow instabilities. *J. Fluid Mech.* **276**, 327–342.

Balaras, E., Piomelli, U. & Wallace, J. M. 2001 Self-similar states in turbulent mixing layer. *J. Fluid Mech.* **446**, 1–24.

Balsa, T. F. 1987 On the spatial instability of piecewise linear free shear layers. *J. Fluid Mech.* **174**, 553–563.

Batchelor, G. G. 1967 *An Introduction to Fluid Dynamics*. Cambridge University Press.

Betchov, R. & Criminale, W. O. 1966 Spatial instability of the inviscid jet and wake. *Phys. Fluids* **9**, 359–362.

Caulfield, C. P. 1994 Multiple linear instability of layered stratified shear flow. *J. Fluid Mech.* **258**, 255–285.

Caulfield, C. P. & Peltier, W. R. 2000 The anatomy of the mixing transition in homogeneous and stratified free shear layers. *J. Fluid Mech.*, 3**43**, 1–47.

Chen, D., Jirka, G. H. 1998 Linear stability analysis of turbulent mixing layers and jets in shallow water layers. *J. Hydraul. Res.* **36**, 815–830.

Cohen, J. & Wygnanski, I. 1987 The evolution of instabilities in the axisymmetric jet. Part 1. The linear growth of disturbances near the nozzle. *J. Fluid Mech.* **176**, 191–219.

Comte, P., Lesieur, M., Laroche, H. & Normand, X. 1989 Numerical simulations of turbulent plane shear layers. In *Turbulent Shear Flows 6* (ed. J. C. André, J. Custeix, F. Durst *et al.*), pp. 360–380. Springer.

Cortesi, A. B., Smith, B. L., Yadigaroglu, G. & Banerjee, S. 1999 Numerical investigation of the entrainment and mixing processes in neutral and stably-stratified mixing layers. *Phys. Fluids* **11**, 162–185.

Cortesi, A. B., Yadigaroglu, G. & Banerjee, S. 1998 Numerical investigation of three-dimensional structures in stably-stratified mixing layers. *Phys. Fluids* **10**, 1449–1473.

Davis, P. A. & Peltier, W. R. 1977 Effects of dissipation on parallel shear instability near the ground. *J. Atmos. Sci.* **34**, 1868–1884.

Defina, A., Lanzoni, S. & Susin, F. M. 1999 Stability of a stratified viscous shear flow. *Phys. Fluids* **11**, 344–355.

Drazin, P. G. 1958 The stability of a shear layer in an unbounded heterogeneous inviscid fluid. *J. Fluid Mech.* **4**, 214–224.

Drazin, P. G. & Reid, W. H. 1984 *Hydrodynamic Stability*. Cambridge University Press.

Estevadeordal, J. & Kleis, S. J. 2002 Influence of vortex-pairing location on the three-dimensional evolution of plane mixing layers. *J. Fluid Mech.* **462**, 43–77.

Freymuth, P. 1966 On transition in a separated boundary layer. *J. Fluid Mech.* **25**, 683–704.

Gaster, M. 1962 A note on the relation between temporally-increasing and spatially-increasing disturbances in hydrodynamic stability. *J. Fluid Mech.* **14**, 222–224.

Gaster, M. 1968 Growth of disturbances in both space and time. *Phys. Fluids* **11**, 723–727.

Gaster, M., Kit, E. & Wygnanski, I. 1985 Large-scale structures in a forced turbulent mixing layer. *J. Fluid Mech.* **150**, 23–39.

Gelfgat, A. Yu. 2001 Two- and Three-dimensional instabilities of confined flows: numerical study by a global Galerkin method. *Comput. Fluid Dyn. J.* **9**, 437–448.

Ghoniem, A. F. & Ng, K. K. 1987 Numerical study of the dynamics of a forced shear flow. *Phys. Fluids* **30**, 706–721.

Haigh, S. P. 1995 Non-symmetric Holmboe waves. PhD thesis, University of British Columbia.

Haigh, S. P. & Lawrence, G. A. 1999 Symmetric and non-symmetric Holmboe instabilities in an inviscid flow. *Phys. Fluids* **11**, 1459–1468.

Hajj, M. R. 1997 Stability characteristics of a periodically unsteady mixing layer. *Phys. Fluids* **9**, 392–398.

Hazel, P. 1972 Numerical studies of the stability of inviscid shear flows. *J. Fluid Mech.* **51**, 39–61.

Hogg, A. McC. & Ivey, G. N. 2003 The Kelvin-Helmholtz to Holmboe instability transition in stratified exchange flows. *J. Fluid Mech.* **477**, 339–362.

Holmboe, J. 1962 On the behaviour of symmetric waves in stratified shear layers. *Geophys. Publ.* **24**, 67–113.

Howard, L. N. 1961 Note on a paper of John W. Miles. *J. Fluid Mech.* **10**, 509–512.

Klaassen, G. P. & Peltier, W. R. 1985. The onset of turbulence in finite amplitude Kelvin-Helmholtz billows. *J. Fluid Mech.* **155**, 1–35.

Knio, O. M. & Ghoniem, A. F. 1991 Three-dimensional vortex simulation of rollup and entrainment in a shear layer. *J. Comput. Phys.* **97**, 172–223.

Koppel, D. 1964 On the stability of flow of a thermally stratified fluid under the action of gravity. *J. Math. Phys.* **7**, 963–982.

Korzak, K. Z. & Wessel, R. A. 1989 Mixing control in a plane shear layer. *AIAA J.* **27**, 1744–1751.

Kuznetsov, Y. A. 2004 *Elements of Applied Bifurcation Theory*. Applied Mathematical Sciences, vol. 112, Springer.

Lawrence, G. A., Browand, F. K. & Redekopp, L. G. 1991 The stability of a sheared density interface. *Phys. Fluids* A **3**, 2360–2370.

Lie, K. H. & Riahi, D. N. 1988 Numerical solution of the Orr-Sommerfeld equation for mixing layers. *Intl J. Engng Sci.* **26**, 163–174.

Mallier, R. 1995 The nonlinear temporal evolution of a disturbance to a stratified mixing layer. *J. Fluid Mech.* **29**, 287–297.

Michalke, A. 1965 On spatially growing disturbances in an inviscid shear layer. *J. Fluid Mech.* **23**, 521–544.

Miksad, R. W. 1972 Experiments on the nonlinear stages of free-shear-layer transition. *J. Fluid Mech.* **56**, 695–719.

Miles, J. W. 1961 On the stability of heterogeneous shear flows. *J. Fluid Mech.* **10**, 496–508.

Miller, R. S., Harstad, K. G. & Bellan, J. 2001 Direct numerical simulation of supercritical fluid mixing layers applied to heptane-nitrogen. *J. Fluid Mech.* **436**, 1–39.

Monkewitz, P. A. & Huerre, P. 1982 Influence of the velocity ratio on the spatial instability of mixing layers. *Phys. Fluids* **25**, 1137–1143.

Nayfeh, A. H. & Padhye, A. 1979 Relation between temporal and spatial stability in three-dimensional flows. *AIAA J.* **17**, 1084–1090.

Nishida, S. & Yoshida, S. 1987 Stability and eigenfumctions of disturbance in stratified two-layer flows. *Proc. Intl Symp. on Stratified Flows, Pasadena, CA, 3–5 February 1987*, pp. 28–34.

Nishida, S. & Yoshida, S. 1990 Influence of the density and velocity profiles on calculated instability characteristics in an inviscid two-layer shear flow. *J. Hydrosci. Hydraul. Engng* **7**, 61–68.

Ortiz, S., Chomaz, J.-M. & Loiseleux, T. 2002 Spatial Holmboe instability. *Phys. Fluids* **14**, 2585–2597.

Patnaik, P. C., Sherman, F. S. & Corcos, G. M. 1976 A numerical simulation of Kelvin-Helmholtz waves of finite amplitude. *J. Fluid Mech.* **73**, 215–240.

Pawlak, G. & Armi, L. 1998 Vortex dynamics in a spatially accelerating shear layer. *J. Fluid Mech.* **3765**, 1–35.

Peng, M. S. & Williams, R. T. 1987 On the transformations between temporal and spatial growth rates. *J. Atmos. Sci.* **44**, 2668–2673.

Peltier, W. R. & Caulfield, C. P. 2003 Mixing efficiency in stratified shear flows. *Annu. Rev. Fluid Mech.* **35**, 135–167.

Peltier, W. R. & Scinocca, I. F. 1990 The origin of severe downs lope windstorm pulsations. *J. Atmos. Sci.* **47**, 2853–2870.

Pruett, C. D. 1989 A fast algorithm for simulation of a spatially evolving two-dimensional planar mixing layer. *Comput Meth. Appl. Mech. Engng* **76**, 275–298.

Rajaee, M. & Karlsson, K. F. 1992 On the Fourier space decomposition of free shear flow measurements and mode degeneration in the pairing process. *Phys. Fluids* A **4**, 321–339.

Reinaud, J., Joly, L. & Chassaing, P. 2000 The baroclinic secondary instability of the two-dimensional shear layer. *Phys. Fluids* **12**, 2489–2505.

Roychowdhury, A. P. & Sreedhar, B. N. 1992 Gaster's transform. *AIAA J.* **30**, 2776–2778.

Scinocca, J. F. 1995 The mixing of mass and momentum by Kelvin-Helmholtz billows. *J. Atmos. Sci.* **52**, 2509–2530.

Smyth, W. D. 2003 Secondary Kelvin-Helmholtz instability in weakly stratified shear flow. *J. Fluid Mech.* **497**, 67–98.

Smyth, W. D. 2004 Kelvin-Helmholz billow evolution from a localized source. *Q. J. R. Met. Soc.* **130**, 2753–2766.

Smyth, W. D., Klaassen, G. P. & Peltier, W. R. 1988 Finite amplitude Holmboe waves. *Geophys. Astrophys. Fluid Dyn.* **43**, 181–222.

Smyth, W. D. & Moum, N. 2000*a* Length scales of turbulence in stably stratified mixing layers. *Phys. Fluids* **12**, 1327–1342.

Smyth, W. D. & Moum, N. 2000*b* Anisotropy of turbulence in stably stratified mixing layers. *Phys. Fluids* **12**, 1343–1362.

Smyth, W. D., Moum, J. N. & Caldwell, D. R. 2001 The efficiency of mixing and turbulent patches: inferences from direct simulations and microstructure observations. *J. Phys. Oceanogr.* **31**, 1969–1992.

Smyth, W. D. & Peltier, W. R. 1989 The transition between Kelvin-Helmholtz and Holmboe instability: an investigation of the overreflection hypothesis. *J. Atmos. Sci.* **46**, 3698–3720.

Smyth, W. D. & Peltier, W. R. 1990 Three-dimensional primary instabilities of a stratified, dissipative, parallel flow. *Geophys. Astrophys. Fluid Dyn.* **52**, 249–261.

Smyth, W. D. & Peltier, W. R. 1991 Instability and transition in finite-amplitude Kelvin-Helmholtz and Holmboe waves. *J. Fluid Mech.* **228**, 387–415.

Smyth, W. D. & Peltier, W. R. 1994 Three-dimensionalization of barotropic vortices on the $f$-plane. *J. Fluid Mech.* **265**, 25–64.

Smyth, W. D. & Winters, K. B. 2003 Turbulence and mixing in Holmboe waves. *J. Phys. Oceanogr.* **33**, 694–711.

Soh, W. Y. 1994 Numerical simulation of free shear flow and far field sound pressure directivity. *Intl J. Numer. Meth. Fluids* **18**, 337–359.

Staquet, C. 1995 Two-dimensional secondary instabilities in a strongly stratified shear layer. *J. Fluid Mech.* **296**, 73–126.

Staquet, C. 2000 Mixing in a stably stratified shear layer: two- and three-dimensional numerical experiments. *Fluid Dyn. Res.* **27**, 367–404.

Sutherland, B. R. & Peltier, W. R. 1992 The stability of stratified jets. *Geophys. Astrophys. Fluid Dyn.* **66**, 101–131.

Vreman, B., Geurts, B. & Kuerten, H. 1997 Large-eddy simulation of the turbulent mixing layer. *J. Fluid Mech.* **339**, 357–390.

Weisbrot, I. & Wygnanski, I. 1988 On coherent structures in a highly excited mixing layer. *J. Fluid Mech.* **195**, 137–159.

Wilson, R. V. & Demuren, A. O. 1996 Two-dimensional spatially-developing mixing layers. Numer. *Heat Transfer* A **29**, 485–509.

Wygnanski, I., Champagne, F. & Marasli, B. 1986 On the large-scale structures in two-dimensional, small-deficit, turbulent wakes. *J. Fluid Mech.* **168**, 31–71.

Yih, C.-S. 1955 Stability of two-dimensional parallel flows for three-dimensional disturbances. *Q. Appl. Maths* **12**, 434–435.

Zhu, D. Z. & Lawrence, G. A. 2001 Holmboe's instability in exchange flows. *J. Fluid Mech.* **429**, 391–409.